Renewable Energy 190 (2022) 232–250

Contents lists available at ScienceDirect

Renewable Energy

journal homepage: www.elsevier.com/locate/renene

Robust validation of a generalised actuator disk CFD model for tidal turbine analysis using the FloWave ocean energy research facility

Charles E. Badoe [a], Matt Edmunds [a], Alison J. Williams [a, *], Anup Nambiar [b], Brian Sellar [b], Aristides Kiprakis [b], Ian Masters [a]

[a] Energy and Environment Research Group, Zienkiewicz Centre for Computational Engineering, College of Engineering, Bay Campus, Swansea University, SA1 8EN, Wales, UK
[b] School of Engineering, University of Edinburgh, EH9 3DW, Scotland, UK

ARTICLE INFO

Article history:
Received 15 October 2020
Received in revised form
12 January 2022
Accepted 19 March 2022
Available online 25 March 2022

Keywords:
FloWave
GAD-CFD
Blade element momentum
Tidal energy
Tidal turbine
Horizontal axis turbine

ABSTRACT

Coupled blade element momentum-computational fluid dynamic (BEM-CFD) approaches have been extensively used to study tidal stream turbine performance and wake development. These approaches have shown to be accurate when compared to tests conducted in tow-tanks or in regulated flumes with uniform flows across the turbine. Whilst such studies can be very useful, it is questionable as to what extent the results would differ in a larger scale environment where the flow is more representative of real-world conditions, being either unsteady or non-uniform. In this work, the effectiveness of a generalised actuator disk-computational fluid dynamics (GAD-CFD) approach in accurately capturing fluid-machine interaction for single and multiple tidal energy converters models is further assessed. A unique large-scale experimental facility, FloWave, has been used to conduct physical testing of three instrumented model tidal energy converters of rotor diameter 1.2 m under differing turbine layouts and realistic scaled environmental conditions. These large-scale tests provide a unique dataset against which this work's numerical simulations have been extensively validated. Comparisons between the tank and GAD-CFD approach show good agreement, particularly when comparing modelled to measured thrust, and enabled an evaluation of the effects of turbine spacing and arrangement on turbine performance and flow-field response.

1. Introduction

Tidal stream power generation has emerged in recent years as a potentially reliable form of renewable energy due to the predictability of tidal periods and magnitudes [1]. Many tidal sites across the world are being identified and tidal current turbines installed in small arrays to generate and export electricity to local networks [2]. Academic interest in the sector is growing in parallel to the growth of industrial investment. A number of experimental and numerical studies have been conducted to improve our understanding of these devices, ranging from device design, through environmental impact, to the hydrodynamic performance of devices, individually and in arrays. The works by Selig et al. [3], Bahaj et al. [4], Stallard et al. [5], and Mycek et al. [6,7], are all suitable experiments which can be utilised for the assessment of turbine performance. These data sets can also be used to validate numerical models representing the turbine performance characteristics, thus allowing local turbine flow details to be examined, which are difficult to obtain using experiments.

Computational fluid dynamics (CFD) has been used, through a number of approaches, to predict the response of tidal turbines, including their loading, performance and wake generation, under complex environmental inflow conditions. Each approach has advantages and disadvantages, with the main balance being a trade off between detailed simulation of the physics and the computational time and resources required to achieve a result [8].

At the smallest and most detailed scale, fully resolved turbine geometry models have been used to provide insight into the development of the wake flow downstream of a device [9–12]. However, these approaches require small time steps due to restrictions imposed by explicitly solving the turbine flow, thus

* Corresponding author.
E-mail address: alison.j.williams@swansea.ac.uk (A.J. Williams).

https://doi.org/10.1016/j.renene.2022.03.109

placing a high demand on computation. As such, they are not feasible when considering simulation of large array of full scale turbines at a useful level of approximation for studying turbine performance and wake flow. In addition, high computational cost restricts simulation of a wide range of incident environmental conditions, which are known, for tidal energy sites, to be highly variable resulting from complex combinations of waves, currents and turbulence. Computations of these nature are often performed using representative turbine models or body force methods.

The level of complexities in the body force methods varies from prescribing the body forces [13,14], through to coupling a more complex turbine performance code which accounts for the variation along the blade geometry such as the Blade Element Momentum Theory CFD (BEM-CFD) approach [15–17]. The approach utilises a radially varying set of blade characteristics, uniformly distributed in an axial direction. Hence, computational cells at the same radius from the rotor centre have the same properties, however, as the flow varies from cell to cell, the resultant forces on the fluid also vary. It follows that the BEM-CFD approach can also be useful for predicting turbine-turbine interactions with respect to positioning. These models can also allow the local environment to be simulated providing a comprehensive study of a tidal farm [18]. With this in mind, the use of BEM-CFD approach which accurately predicts device operation without the extensive computational cost of expensive fully resolved turbine geometry models would be of great benefit to the industry.

A steady state BEM-CFD [19] was used to predict the effect of rotor on the fluid domain. The authors then examine the power output of rows of turbines where each row is reduced in performance by a constant factor. This type of model has also been used to study wake length and inflow characteristics [20], the effect of accelerating flows [21] and the interaction of arrays of turbines [16]. The application of tip loss corrections and downwash pertinent to a CFD type model representation takes this approach further. This extension, the Generalised Actuator Disk (GAD-CFD) has provided confidence when applied to laboratory scale flume studies [22]. The benefit of the GAD-CFD approach, with respect to computational cost, is unequivocal. This technique allows us to move into the realms of array interaction modelling and site design at a more reasonable level of cost.

To further assess the performance of the GAD-CFD approach, in terms of modelling accuracy and capacity to model multiple turbines in more varied configurations, new validation datasets are required. To secure these datasets the numerical simulation work was coordinated with physical tank-testing conducted at the FloWave facility [23] to create replicate domains which enable detailed cross-comparison of results.

FloWave was specifically designed to enable the testing of offshore renewable energy devices in arrays, featuring a large 25 m diameter round tank, 2 m working depth and the ability to create combined waves and currents from any direction. The FloWave experiments enable both an increase in the underlying flow-speeds and scale of model testing (reducing uncertainties arising from scale and friction effects and allowing more and higher fidelity model sensing), and comparisons between tidal energy converter farm layouts.

The aim of the present study is to (i) assess the performance of the GAD-CFD approach for the prediction of the loadings and wake details through detailed comparison with experimental FloWave data and (ii) analyse any compromises required for such a model and the computational cost necessary to make such assessment possible.

The remainder of this paper is organised as follows: In §2 we present the experimental approach, while the mathematical and numerical details of the GAD-CFD is explained in detail in §3. Turbulent Lift and Drag Data and the sensitivity of the GAD-CFD methodology are explained in §4 and §5 respectively. Results are presented in §6 for a tank only baseline model as well as single and three turbine array cases. Comparison is made to the wake profile and turbine loads. Summary and concluding remarks are presented in §7 and §8 respectively.

2. Experimental set-up and methods

2.1. Test facility

All the experimental work reported in this paper was carried out at the Flowave Ocean Research facility located at the University of Edinburgh, UK [23–25]. Flowave (see Fig. 1) is a circular, combined wave and current tank, with a diameter of 25 m and an operating water depth of 2 m. In the centre of the tank is a 15 m diameter, raisable floor that provides access to the floor for model and instrumentation installation. A movable gantry, that spans the diameter of the tank, provides access to the floor. As shown in Fig. 1, beneath the floor, in the plenum chamber along the entire tank circumference, are 28 impeller units that create a re-circulating flow system [26]. This arrangement of impellers allows the generation of a predominantly straight flow in any direction across the central test area of the tank [27].

The maximum current velocity achievable is 1.6 m/s. There is no facility available to control the turbulence intensity of the currents generated and is around 7% for the flow velocity used in these experiments. This is approximately representative of some real-world tidal sites for periods of fast flows [28]. Due to the nature of flow generated in a circular tank, there is some spatial variation of the mean flow and turbulence intensity across the tank area, which have been characterised in Refs. [27,29]. [27] shows a 50 m^2 region of relatively straight uniform flow ($\pm$10%) in the tank centre. The turbines, used in this test campaign, were installed in this region of the tank.

The flow in the tank was set at the design flow speed of the turbine model [33], nominally 0.8 m/s inflow at a hub-height location without the turbine installed in the tank, which is consistent with previous tests with a single turbine [34]. This corresponds to a full-scale flow speed of 3.1 m/s. The chord-length Reynolds numbers vary between 0.5×10^5 (root) and 2.5×10^5 (tip). From previous experiments, the power and thrust coefficients (C_P and C_T) for the model turbine rotor were found to be Reynolds invariant above a current velocity of 0.6 m/s.

2.2. Turbines and instrumentation

An array of three turbines was used in the tests (see Fig. 2), one fully instrumented primary turbine with two additional turbines upstream to alter the inflow conditions as would happen in an array. The turbines are generic bed-mounted, fixed-pitch, three-bladed horizontal axis design. The turbine models are 1:15 scale, corresponding to an 18 m diameter prototype. Full details of the turbine design used for the test, including on-board instrumentation is described in Refs. [31–33]. Table 1 also summarizes the principal dimensions of the turbine.

The primary turbine (red fairing in Fig. 2) had an array of instrumentation, including sensors to measure the streamwise root bending moment for each blade RBM, torque Q and thrust T on the rotor. The front two turbines were identical to the primary turbine but did not have RBM sensors on them. The generators in the turbines were simulated using permanent magnet servo motors, directly connected to the rotor shafts. They provide a controllable resisting torque to the hydrodynamic torque imparted by the interaction of the flow and the turbine rotor. Rotor angular

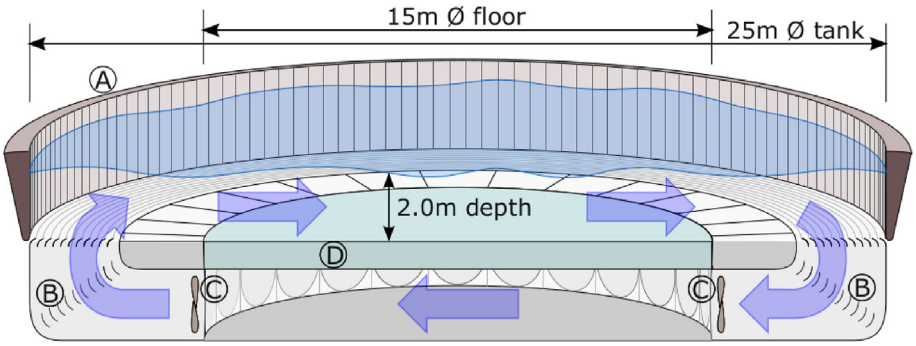

Fig. 1. Sectional schematic of FloWave basin showing: (A) wavemaker paddles around circumference; (B) turning vanes and flow conditioning filters; (C) current drive impeller units; (D) buoyant raisable floor (15 mø) below test area [29].

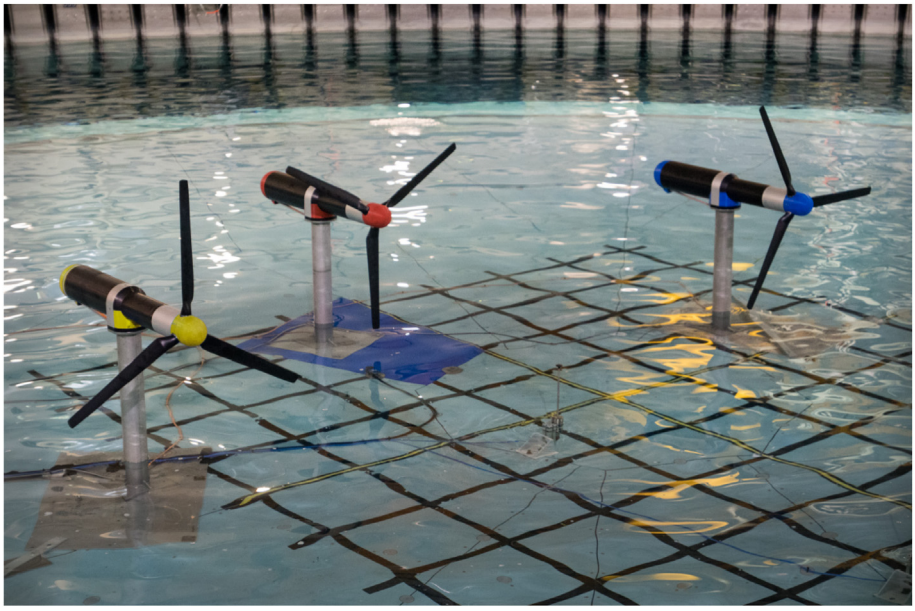

Fig. 2. Turbine array installed in FloWave, as the floor descends after installation. Fully instrumented primary turbine (red fairing) in the centre between front turbines (yellow and blue). Array layout and configurations tested are shown in Fig. 3. Grid on tank floor relative to tank centre, with 0.5 m spacing [29].

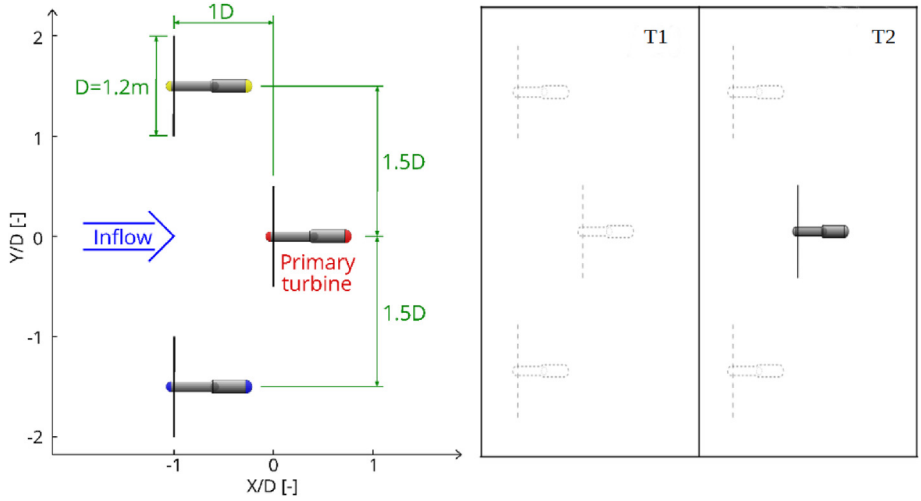

Fig. 3. (left) Three turbine array layout, and (right) two configurations tested: T1 empty tank, T2 primary turbine only [30].

Table 1
Turbine dimensions [30].

Parameter	*Dimension[m]*
Rotor diameter	1.2 (1D)
Nacelle length	1.03
Nacelle diameter, hub to tower	0.12
Nacelle diameter, beyond tower	0.16
Hub height	1.0 (0.83D)
Tower diameter	0.102
Distance from rotor plane to tower axis	0.486 (0.4D)

positions, θ, were obtained from the motor encoders. The turbines were operated in speed control mode over a range of different tip speed ratios.

The primary turbine, both in the single turbine and array tests, was mounted on a bottom-mounted six axes (6 DOF) load cell to measure the forces and moments on the entire turbine structure (including the blades, the turbine nacelle and the tower). The load-cell was flush-mounted within the tank floor, which dictates the location of this turbine, with the tower offset 1.6 m downstream and 0.5 m to the side of the tank centre.

2.3. Array configuration

To investigate array effects on the primary turbine, two additional identical turbines were placed upstream to alter the inflow, as shown in Fig. 3. This was based on an array configuration tested numerically using Blade Element Momentum Theory-Computational Fluid Dynamics (BEM-CFD) in Ref. [18]. The hubs of these two upstream turbines were 1 D upstream and 1.5 D either side of the primary turbine, giving a transverse separation of 3 D. This configuration was shown in Ref. [18] to accelerate the flow experienced by the rear turbine and improve its performance. Additionally, the front row being only 1 D in front of the primary turbine, means that the rear turbine is not in the wake of the front two turbines. Flow measurements and loading tests were conducted for two array configurations as shown in Fig. 3: (left image) the full three turbine array and T2 with only the primary turbine installed. For baseline comparison, the flow was measured in the tank without any turbines installed, shown as configuration T1 in Fig. 3.

The blockage ratio of the 1.2 m diameter turbine at Flowave, defined as the turbine rotor plane area divided by the tank cross-section area, is approximately 2.3%. The vertical blockage, $D/h = 0.6$ is representative of real deployments [28,35]. The horizontal blockage $D/w = 0.048$, where w is the width of the basin, is low due to the large horizontal dimension of the tank. These parameters show that any unrealistic blockage effects are not expected during single turbine testing. For the three-turbine array, the blockage is higher at 6.9%, but the horizontal dimension of the tank is large enough to remove any impact on the bypass flow around the array.

The local coordinate system used for these tests has the origin at the primary turbine hub, with X positive in the streamwise direction. Distances are normalised by the turbine diameter D of 1.2 m.

2.4. Flow measurement

Flow measurements at different points in the flow field were made at hub height (1 m above the tank floor) to characterise the inflow, the wake and the flow in the region between the turbines. These measurements were made using a Nortek Vectrino Profiler Acoustic Doppler Velocimeter (ADV) [36] with a sampling rate of 100 Hz. By periodically seeding the tank with neutrally buoyant glass micro-spheres, per-beam correlation values returned by the ADV were maintained at approximately 95%. The velocity range was set to 1.8 m/s to prevent wrapping due to high velocity spikes. At each measurement point, flow was measured for 256 s based on previous work at Flowave [29], after allowing the flow to reach steady state. The measured flow data, with the streamwise, transverse, and vertical velocity components, was then processed to remove outlier spikes using a despiking algorithm [37,38]. Due to time constraints and other investigation priorities, the number and position of flow measurement points varies slightly between array configurations. It was not possible to measure flow within 0.3 m of the turbine rotor.

Table 2 summarizes the specifications of all the instrumentation used in the tests.

3. Numerical Methodology

3.1. Governing equations

The OpenFOAM toolbox [39] is utilised for the model implementation. The OpenFOAM toolkit provides a range of standard solvers which can be modified for use with the additional turbine physics. The additional GAD source terms are implemented in the steady state Reynolds Averaged Navier Stokes (RANS) "simpleFoam" solver. Within the assumption of an incompressible fluid, the set of equations maybe written in the form:

$$\frac{\partial \bar{U}_i}{\partial x_i} = 0 \tag{1}$$

$$\frac{\partial \bar{U}_i}{\partial t} + \frac{\partial \bar{U}_i \bar{U}_j}{\partial x_j} = -\frac{1}{\rho}\frac{\partial \bar{P}}{\partial x_i} + \frac{\partial}{\partial x_j}\left(\nu\left(\frac{\partial \bar{U}_i}{\partial x_j} + \frac{\partial \bar{U}_j}{\partial x_i}\right)\right) - \frac{\partial \overline{u'_i u'_j}}{\partial x_j} + f_i, \tag{2}$$

where x_i represents the Cartesian coordinates (X, Y, Z), U_i is the Cartesian mean velocity components $(\bar{U}_x, \bar{U}_y, \bar{U}_z)$ and f_i includes an additional source representing the disc rotor characteristics. The Reynolds stress is $\overline{u'_i u'_j}$ and must be modelled to close the governing equations by employing an appropriate turbulence model.

The k-ε RNG turbulence model [40] has been used for this work. In this model two equations are solved; k represents the energy contained within the turbulent fluctuations, and ε represents the dissipation rate of this energy. The equations for the transport of these variables are similar in form to the momentum equations. The model has been credible when applied to flows involving large rotating downstream wakes [8,18,22] which is one of the key aspects of the present application.

3.2. GAD-CFD model

Fig. 4 shows how a turbine with three hydrofoils is discretised

Table 2
Description of installed instrumentation including position relative to the turbine rotor plane centre.

Instrument	*Model*	*Parameter*	*SampleRate[Hz]*	*Location[m]*
ADV	Vectrino Profiler	U, V, W	100	$x, y, 0$
TST	UoE	T, Q, RBM, θ	256	0, 0, 0
Load Cell	AMTI OR6-7	$F_X, F_Y, F_Z, M_X, M_Y, M_Z$	256	0.49, 0, −1

* NB: UoE represents University of Edinburgh.

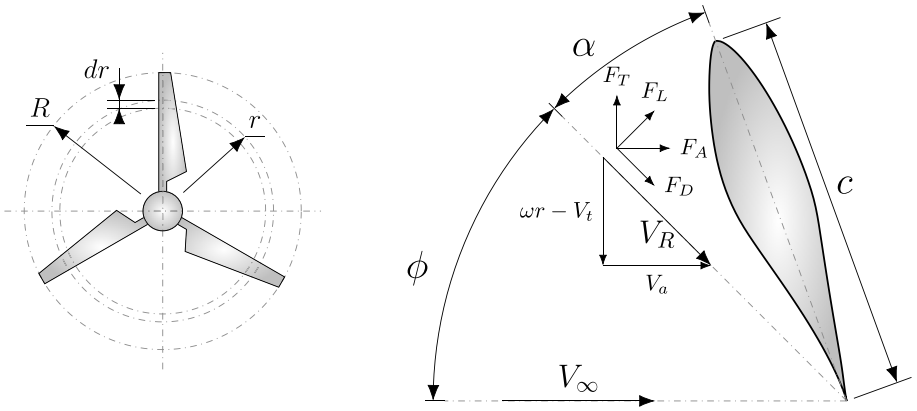

Fig. 4. Generalised Actuator Disk rotor discretisation scheme.

for use with the GAD-CFD approach. The hydrofoil properties are determined at radius r_i, and then averaged over 2π radians. This process is repeated for each hydrofoil element over the interval [r_0, r_{max}].

At any given span wise location r_i, lift is defined as a force perpendicular to the effective flow direction $\boldsymbol{v}_R$, and drag is defined as being parallel to, and opposing, the effective flow direction. The forces can be described, with reference to Fig. 4, by the following equations:

$$F_L = 0.5\,\rho\,|\boldsymbol{v}_R|^2 c\,C_L \tag{3}$$

$$F_D = 0.5\,\rho\,|\boldsymbol{v}_R|^2 c\,C_D \tag{4}$$

where F_L is lift force, and F_D is drag force, ρ is fluid density, $\boldsymbol{v}_R$ is the resultant velocity, c is chord length, C_L is the chord based coefficient of lift, and C_D is the chord based coefficient of drag.

The fluid applies axial and tangential forces to each element as illustrated in Fig. 4. Here F_T is the tangential force and F_A represents the axial force. The lift and drag forces, F_L and F_D respectively, are dependent on C_L and C_D as functions of Reynolds number and the effective angle of attack α. This is the angle between the hydrofoil element and the resultant velocity $\boldsymbol{v}_R$.

Based on the approach in Ref. [41], an axial force on a hydrofoil can be defined as follows:

$$F_A = F_L sin\varphi + F_D cos\varphi \tag{5}$$

and the tangential force on a hydrofoil can be defined as:

$$F_T = F_L cos\varphi - F_D sin\varphi \tag{6}$$

where φ is the flow inclination angle defined by:

$$\varphi = tan^{-1}((\omega r - v_t)\,/\,v_a) \tag{7}$$

Here v_t and v_a are the tangential and axial velocities respectively, and ω is angular velocity [rad/s]. The variation in lift force dF_L, and drag force dF_D, acting along the hydrofoil radius are given as follows:

$$dF_L = 0.5\,\rho\,|\boldsymbol{v}_R|^2 c\,C_L\,dr \tag{8}$$

$$dF_D = 0.5\,\rho\,|\boldsymbol{v}_R|^2 c\,C_D\,dr \tag{9}$$

where:

$$|\boldsymbol{v}_R|^2 = v_a^2 + (\omega r - v_t)^2 \tag{10}$$

Substituting Equations (8) and (9) into Equations (5) and (6) gives the following:

$$S_a = dF_A = 0.5\,\rho\,|\boldsymbol{v}_R|^2 c\,(C_L sin\varphi + C_D cos\varphi)\,dr \tag{11}$$

$$S_t = dF_T = 0.5\,\rho\,|\boldsymbol{v}_R|^2 c\,(C_L cos\varphi - C_D sin\varphi)\,dr \tag{12}$$

To better account for the effect of tip losses on the flow field an additional source term, representing the tip vortex induced downwash $\boldsymbol{w}$ (see Fig. 5), is computed. The downwash force is proportional to the force deflecting the flow around the foil (S_a & S_t), weighted by a downwash distribution function that is calculated by taking into account the blade geometry. A more detailed description of the GAD-CFD model including the extended downwash distribution method is presented in Ref. [22].

4. Turbulent Lift and Drag Data

The prediction of aerofoil characteristics such as lift and drag, with a focus of predicting aircraft performance, is a well studied subject [42]. There is much data available for a range of aerofoils both experimental [43], and analytical [44,45]. However, in most cases the focus is on high Reynolds number predictions of lift and drag within the pre stall set of angles of attack. In addition, the effects of turbulence intensity (TI) on performance is neglected in these studies. This is due to the turbulent fluctuations being small relative to the speed of the aircraft, and thus implies small levels of turbulence.

In contrast to aero environments, lift and drag characteristics in

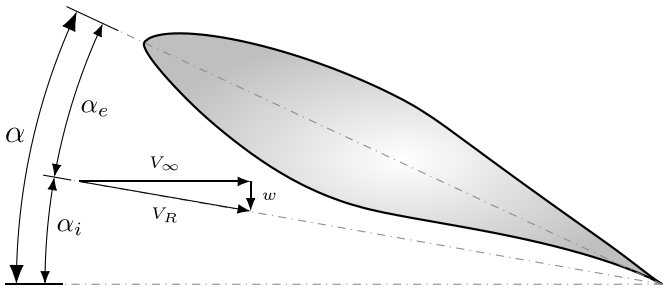

Fig. 5. This diagram highlights the components required to define the induced angle of attack α_i. Where the effective angle of attack is redefined as α_e. The resultant velocity, V_R, shown in this illustration is thus redefined with respect to Fig. 4.

the marine environment are usually a function of high turbulence intensity, often operating at lower Reynolds numbers (particularly in lab scale tests). This makes the use of existing experimental data from the aero environment a source of uncertainty for the accurate prediction of marine environment case studies. In addition to these issues, analytical approaches for predicting lift and drag characteristics generally have problems with the accurate prediction of stall. This is exacerbated at lower Reynolds numbers, and the general inability to predict turbulent effects accurately.

Models that predict horizontal axis tidal turbine performance require coefficients of lift and drag (C_L and C_D) at the correct operating conditions to be assembled and inputted into the given model. This model will perform calculations using this data in conjunction with geometric aspects of the foil, i.e. chord, twist and angle of attack, to compute the local forces.

The fluid velocity is to be determined based on some predefined set of initial/boundary conditions. With this in mind it is thus important to provide accurate inputs to these types of model, and thus it is better to describe C_L and C_D in terms of:

$$LiftForce = 0.5\ \rho\ U^2\ c\ C_L(\alpha, TI, \mathrm{Re}) \tag{13}$$

$$DragForce = 0.5\ \rho\ U^2\ c\ C_D(\alpha, TI, \mathrm{Re}) \tag{14}$$

where TI is turbulence intensity, and Re is Reynolds number.

As the experimental turbines were based on the NACA63812 and 63815 aerofoil sections, a separate CFD study was conducted to determine a set of C_L and C_D curves at a range of Reynolds numbers and turbulence levels required for these sections to use for this study. Fig. 6 compares the NACA63812 and NACA63815 foil sections for TI set to zero percent and TI set to seven percent. It is observed that there is a significant change in performance particularly with respect to drag.

5. The numerical domain: case study-fluid only

5.1. Mesh configuration

All grids were created utilizing both “blockMesh” and “snappyHexMesh” in OpenFOAM version 6.0. The “blockMesh” utility is used to generate an initial block (mesh domain) subdivided into discreet elements. The initial size of the block is set to 30 m square and 4 m deep. The subdivisions are tabulated in Table 3 for the set of meshes used in the mesh sensitivity study (see also subsection 5.3). The discretisation does not use any grading in this case thus “simpleGrading” is set to one. Once the block mesh is generated it is then further refined using the “snappyHexMesh” utility. The “snappyHexMesh” utility approximately conforms to the geometries by iteratively refining the blockMesh and morphing the resulting split-hex mesh to the geometries.

Table 3
Table of initial mesh subdivisions for the set of meshes studied. The total cell count is post refinement using the snappyHexMesh utility.

Mesh	*Subdivisions*	*Total no of cells*
G1	100 × 100 × 30	95686
G2	200 × 200 × 60	766968
G3	300 × 300 × 90	2590032
G4	400 × 400 × 120	6146016
G5	500 × 500 × 150	11998116
G6	600 × 600 × 180	20740456

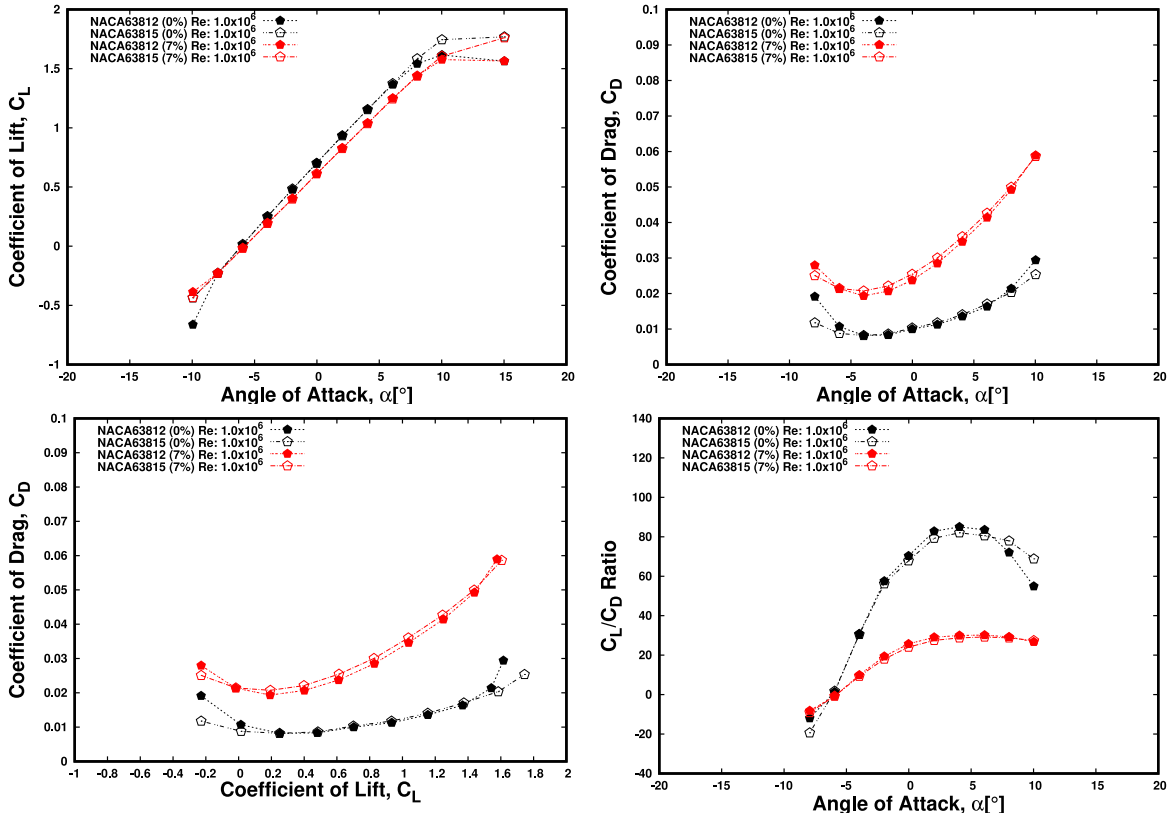

Fig. 6. CFD derived comparison of NACA63812 and NACA63815 foil sections with respect to zero and seven percent TI. Top left is coefficient of lift plotted against angle of attack. Top right is coefficient of drag plotted against angle of attack. Bottom left is coefficient of lift plotted against coefficient of drag. Bottom right is lift drag ratio plotted against angle of attack.

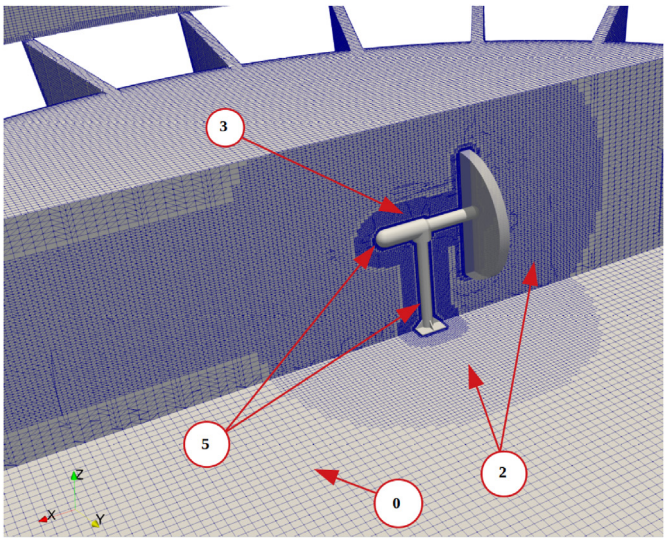

(a)

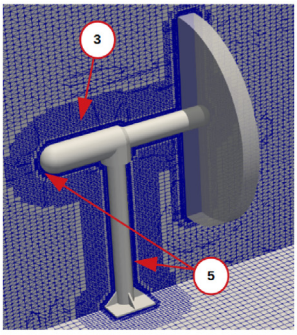

(b)

Fig. 7. [a] Mesh topology generated using a combination of "blockMesh" and "snappyHexMesh" utilities. Note 0 shows the outer/base distribution of cells, while Note 2 shows the level 2 refinements made in the wake region. Note 3 identifies the assembly area refinement, and Note 5 identifies the level 5 assembly region. [b] Zoom in of level 3 and 5 refinements.

The wake region is defined as a cylinder 0.7 m radius, extending from the rotor to 9 m downstream, i.e. to the domain outflow. The refinement level in this region is specified as level 2, i.e. sub-divide the base cell/mesh twice in this region (Note 2 in Fig. 7). The rotor assembly and bladebox is set with a refinement level of 5, i.e. Note 5 in Fig. 7. The region around the rotor assembly (Note 3 in Fig. 7) is set at level 3 up to 0.1 m from the assembly. A reasonable level of detail of the nacelle and support is included in the model as shown in Fig. 7.

5.2. Initial and boundary conditions

Initial and boundary conditions for the set of meshes outlined in subsection 5.1 are described in terms of the CFD case setup in OpenFOAM. The inlet/outlet subsections observed at the edge of the tank (see Figs. 8 and 9) are set to either mass inflow, mass outflow, or no flow depending on the location. The flow rates are set according to Table 4, where in/out location one is located at 12 o'clock, and counted clockwise, see Fig. 9. It was not necessary to model the tank in its entirety i.e. from the inlet/outlet vents only. This reduced the complexity significantly. The tank walls are set to zero velocity and wall functions used for k, ε, and nut. The top of the domain is set to a full slip condition representing the open fluid surface. The initial conditions are mapped to the boundary conditions in all but velocity. The initial velocity condition is set to zero. The kinematic viscosity ν of this problem is set to $1.6667e^{-6}\ m^2\ s^{-1}$.

5.3. Mesh sensitivity studies

Mesh dependency studies of the simulations within the tank was assessed with no turbine present (see T1 in Fig. 3). Velocity and turbulence data were then sampled along the centre of the tank (at hub height, 1 m (0.83D) above the tank floor, see Fig. 10). After running the simulations until the residuals dropped to less than 0.001 for all data fields, the results were compared. The results converge to the answer shown in Fig. 11 after mesh G4, and the general distribution of the velocity and turbulence fields stops evolving, i.e. stabilises, after mesh G4. Based on the study, mesh G4 (see Table 3) representing a reasonable compromise in accuracy and computational cost, was chosen to perform the remaining studies.

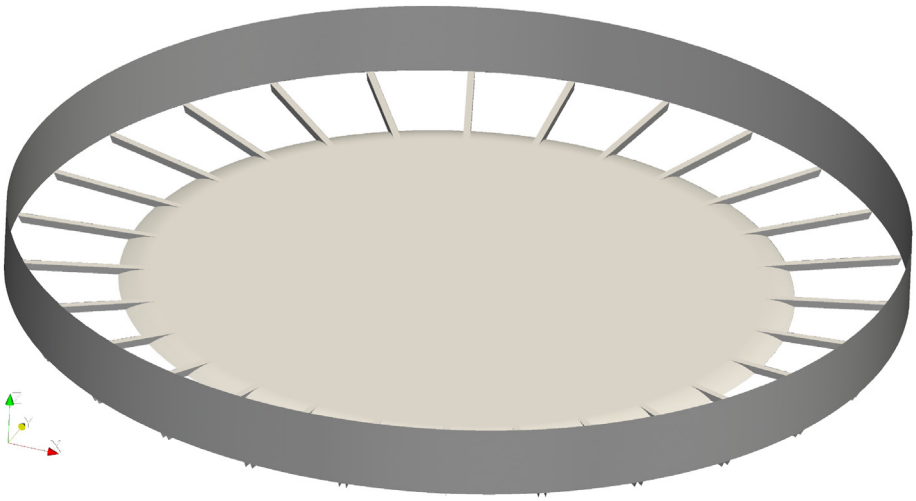

Fig. 8. The geometry of the tank used to build the mesh seen in Fig. 7.

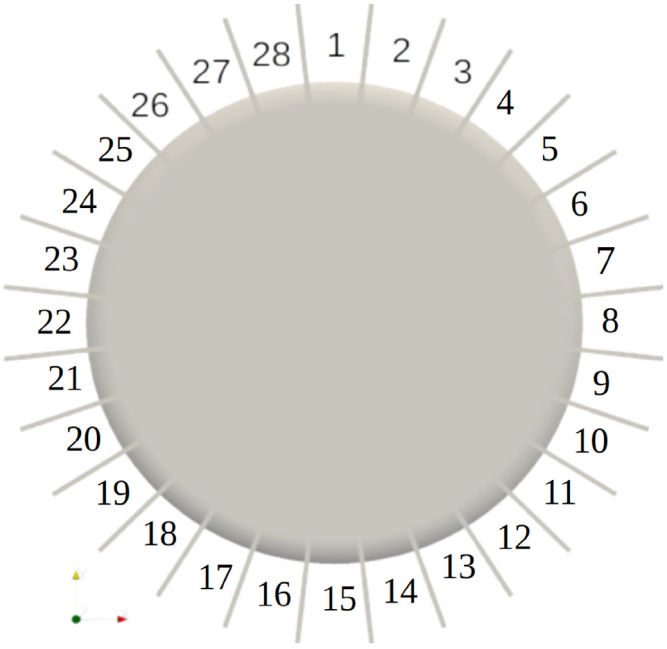

Fig. 9. Enumeration of the in/outlet configuration seen in Fig. 8. This enumeration is used to identify inlet and outlet patches in the numerical model.

Table 4
Table of mass flow rates representing the Flowave tank in cross flow configuration i.e. x axis flow direction, where positive values are inflow and negative is outflow. Both inflow and outflow sum to the same values maintaining conservation of mass.

PatchNo	*MassFlow*[$kg.s^{-1}$]	*PatchNo*	*MassFlow*[$kg.s^{-1}$]
1	0	15	0
2	0	16	0
3	0	17	0
4	−4.0	18	3.150
5	−3.4	19	3.000
6	−2.9	20	2.900
7	−2.1	21	2.825
8	−1.6	22	2.650
9	−2.1	23	2.825
10	−2.9	24	2.900
11	−3.4	25	3.000
12	−4.0	26	3.150
13	0	27	0
14	0	28	0

6. Results

6.1. FloWave tank only (No turbines present)

This section compares the flow measured in the tank without any turbines installed (baseline test) with the GAD-CFD results. Flow velocities and turbulence intensities were evaluated at various locations in the tank at an inflow speed of 0.8 m/s with no turbines present to characterise the inflow and the wake (see Fig. 10). As previously stated, the flow measurements were taken 1 m (0.83D) above the tank floor (at hub height) without the turbines. Fig. 11 compare the profiles of velocity and turbulence intensity along the centerline of the tank at hub height, $y = 0$ m and $z = 1$ m. Strong similarity in the axial velocity and turbulence intensity profiles exist with the experimental data. It appears that the simulation has a slower inflow speed at $x < 0$ m and faster speed at $x > 0$ m compared to the experiment (note, primary turbine location is at $x = 0$).

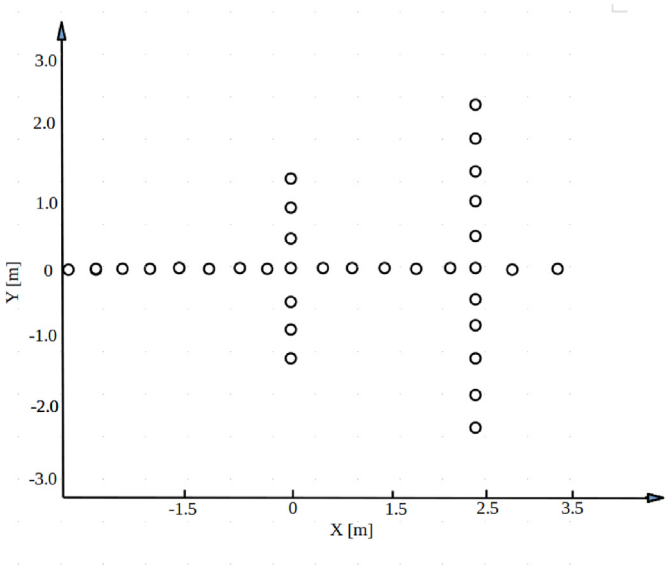

Fig. 10. Schematic showing points at which flow measurements were made. The flow measurements were taken 1 m (0.83D) above the tank floor (at hub height) without the turbines.

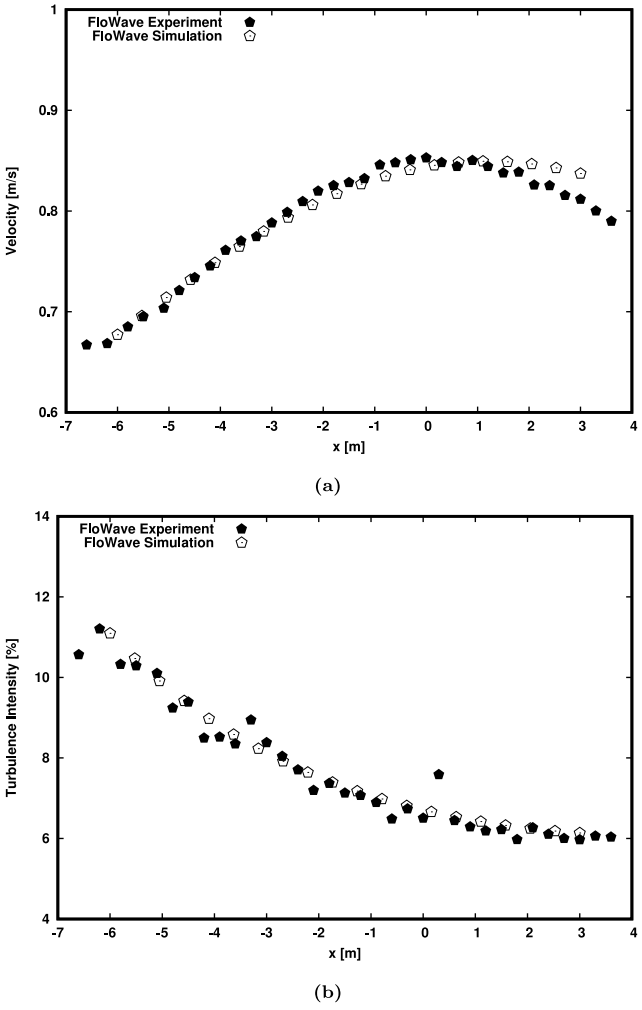

Fig. 11. Velocity magnitude (a) and turbulence intensity (b) plotted against x-axis location along the centre of the tank at hub height, i.e. $y = 0$ *m* and $z = 1$ *m*, No turbine present.

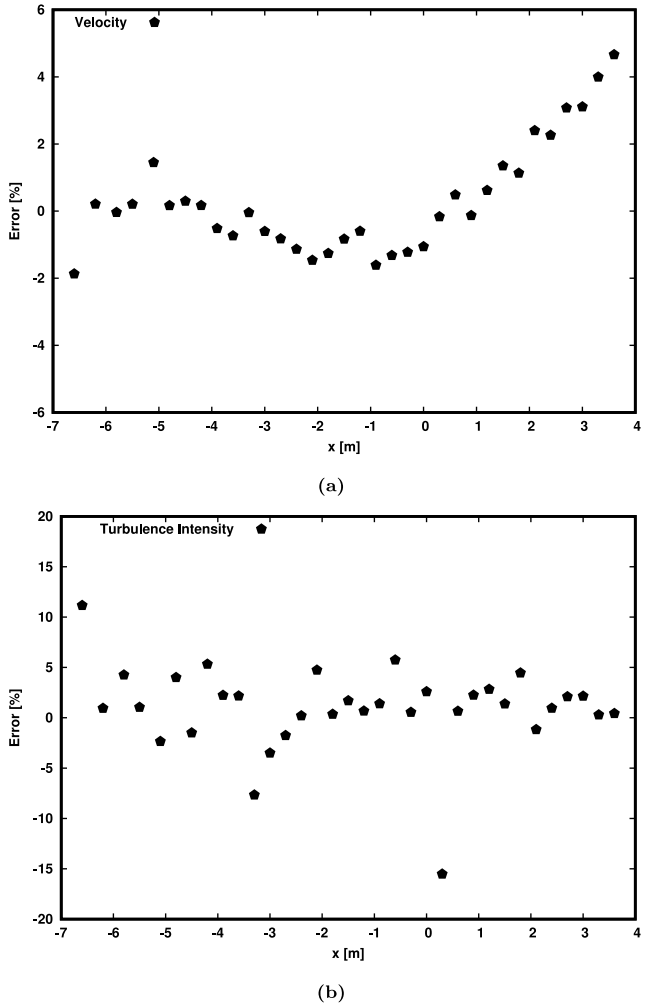

Fig. 12. Percentage error (a) velocity magnitude and (b) turbulence intensity plotted against x-axis location along the centre of the tank at hub height, i.e. $y = 0$ *m* and $z = 1$ *m*, No turbine present.

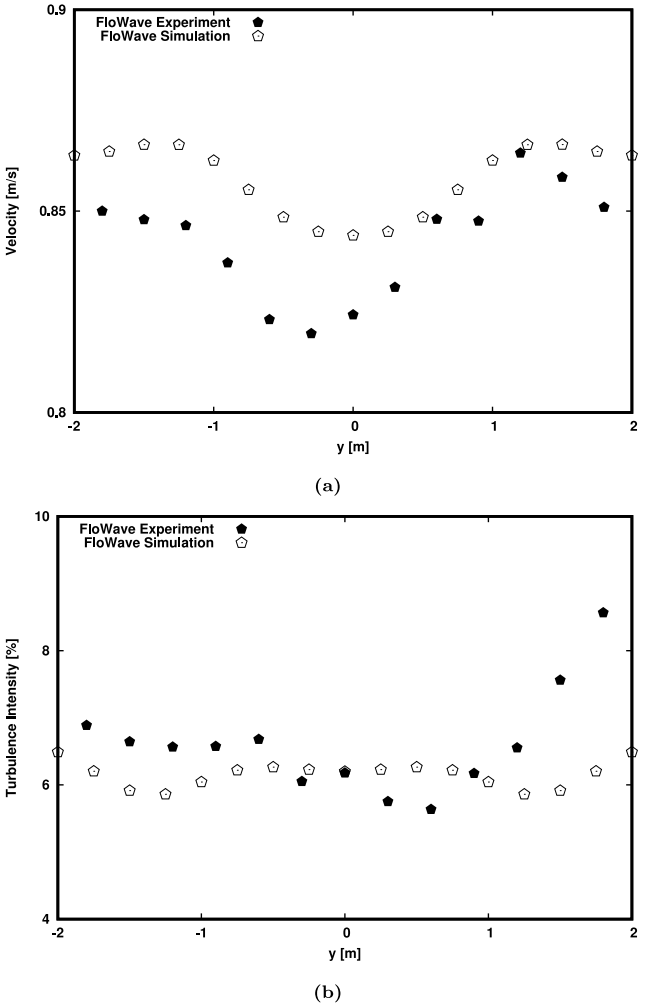

Fig. 13. Velocity magnitude (a) and turbulence intensity (b) plotted against y-axis location across the centre of the tank at hub height, i.e. $x = 0$ *m* and $z = 1$ *m*, No turbine present.

Fig. 12a shows the percentage error in velocity between the computed and measured data at the various sampled locations used for the plots in Fig. 11. The error in velocity reduces closer to the primary turbine location and increases with increase in wake length. There is however a spread in the error in turbulence intensity in Fig. 12b. The difference between the measured and computed averaged lateral velocities and turbulence intensities is 0.3% and 1.2% respectively. The averaged lateral velocities behind the turbine was over-predicted by about 1.2%.

The transverse velocity and turbulence intensity profiles at two different stations is shown in Figs. 13 and 14. The plots show flow development and dissipation across the transverse domain at hub height. Individual flow structures are identified at $x = 0$ m (Fig. 13a) whilst a single flow structure is identified at $x = 2.4$ m (Fig. 14a) in the far downstream region, with the lowest velocity at the centreline. The simulations also show symmetry in both velocity and turbulence intensity profiles, whilst some asymmetry exists in the FloWave experiment, in particular at $x = 2.4$ m in Fig. 14. This may be attributed to the difficulty in controlling the individual impeller units in the tank to generate the required flow across the test area during the experiment, which may have resulted in some variation in mean flow and turbulence intensity across the tank area. The peak velocity in the combined flow structures is higher in the simulation compared to the experiment. The difference between the measured and computed averaged lateral velocities at $x = 0.0$ m and $x = 2.4$ m is 1.8% and 1.7% respectively.

Fig. 15 shows the spatial distribution of velocity magnitude at $z = 1$ m above the tank floor. The inlet flow is directed downstream from the inlet vents, accelerating towards the centre of the tank. Flow is observed to be more uniform in the centre region of the tank than at the edges. Although not shown here strong variations were observed at the same location at $z = 0.1$ m above the tank floor (close to the tank bottom) and $z = 2.0$ m above the tank floor (close to the free surface). Fig. 16 also shows the circulating flow at the tank edges.

6.2. FloWave single rotor

Tip-speed ratio (TSR) sweeps from TSR 4 to 7 were conducted for an isolated rotor case. The number of iterations to convergence ranged from approximately 800 to 1200, where the convergence criteria was set to 1×10^{-3} for all solved equations. Run times ranged from 1.5 to 3.0 wall clock hours for each TSR point, on a 10 core PC workstation.

Coefficient of power C_P and Coefficient of thrust C_T were calculated using the average velocity at the rotors (with rotor removed).

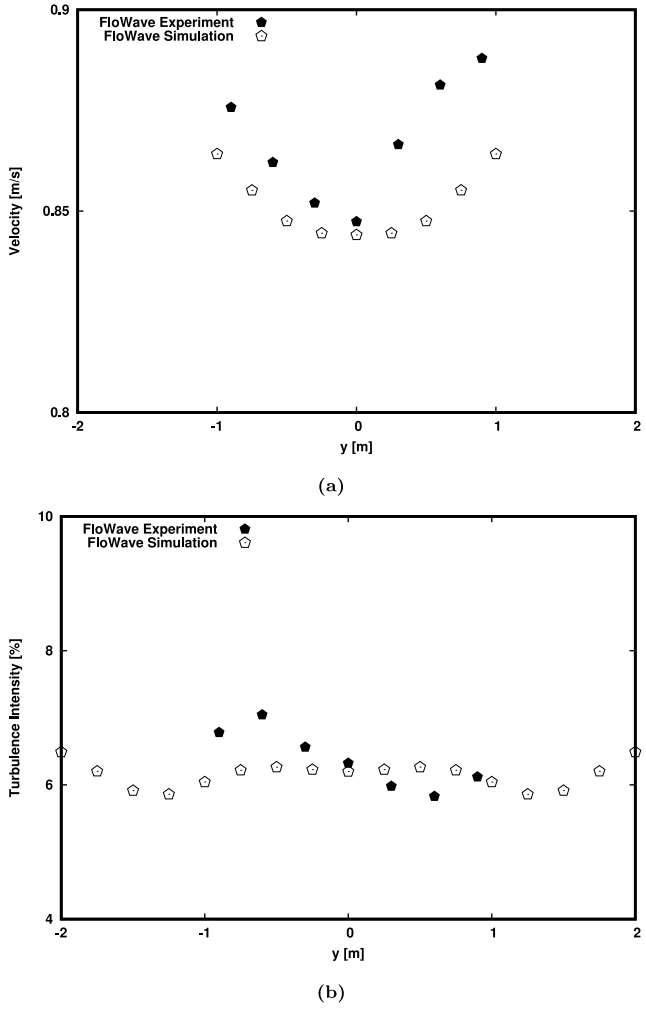

Fig. 14. Velocity magnitude (a) and turbulence intensity (b) plotted against y-axis location across the wake region, i.e. $x = 2.4\ m$ and $z = 1\ m$, No turbine present.

Usually when GAD-CFD is applied, the velocity far upstream or at the inlet is assumed to represent the freestream velocity. However, due to the spatially varying nature of the flow being considered, this would be unrepresentative of the flow at the rotor and hence, the velocity at the rotor location based on the rotorless case, was used. Fig. 17 compares the GAD-CFD performance prediction with the experimental data from the FloWave tank in terms of TSR.

It can be seen that the distribution of power and thrust correlate well with the experimental results. An under prediction of power can be seen in the C_P curve as well as slight over prediction of thrust, especially at TSR $>$ 5. The GAD-CFD model only reports thrust acting directly on the rotor, thus a correction needs to be calculated considering the fluid drag acting on the assembly. This issue was examined in Ref. [46] and demonstrates good correlation for the combined results of thrust. RANS based models including the GAD-CFD model are known to under-predict how much of the energy exerted on the turbine will be converted into rotation on the blades and hence useful power. This has also been reported by Refs. [47,48]. C_P under prediction may also be attributed to variations in local flow directions at the blades and numerical rounding in the model. With this in mind the thrust and power characteristics correlate well and show a similar trend to the observations of the experimental results.

Line samples of velocity and turbulence data were also taken in

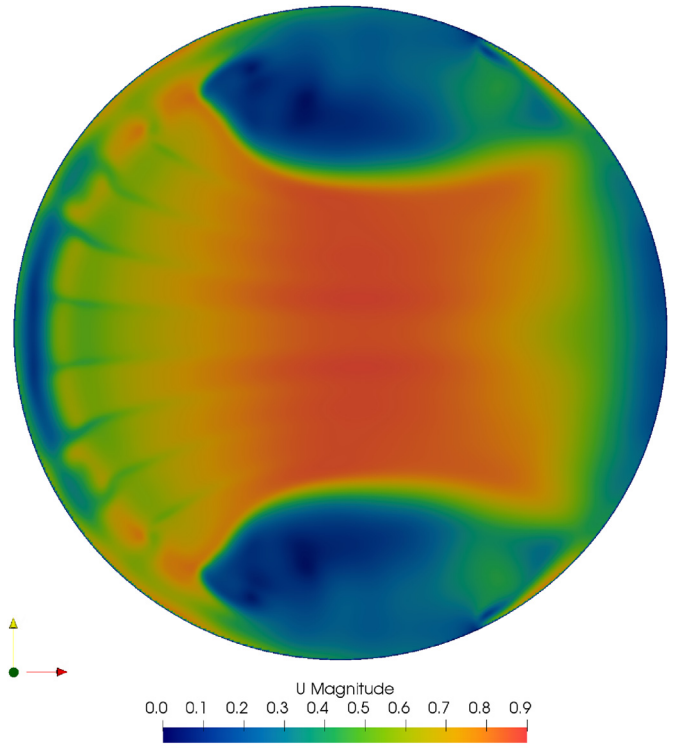

Fig. 15. Velocity magnitude $[0 \ldots 0.9] m.s^{-1}$ taken at hub height (1 m above the tank floor) through the domain. The cross flow direction is from left to right in this view, i.e. x-axis.

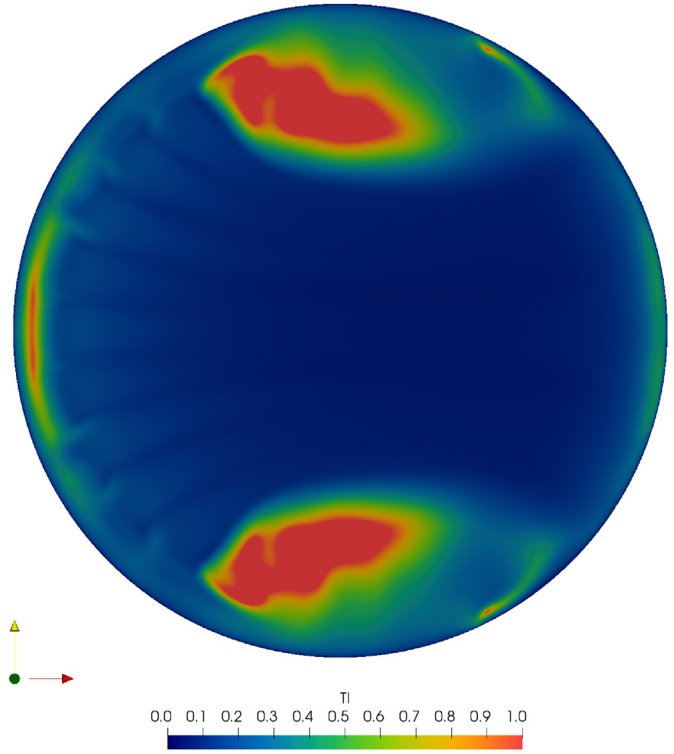

Fig. 16. Turbulence intensity in the range [0 … 1] taken at hub height (1 m above the tank floor) through the domain, where 1 equates to 100% TI. The cross flow direction is from left to right in this view, i.e. x-axis.

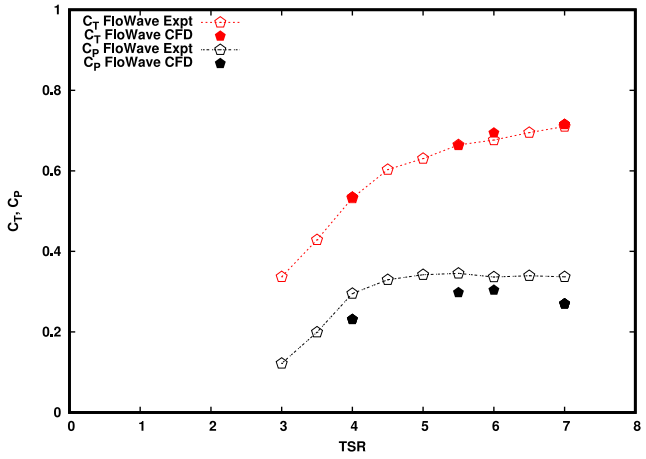

Fig. 17. Comparison of predicted C_P and C_T for the single rotor at a range of TSR's.

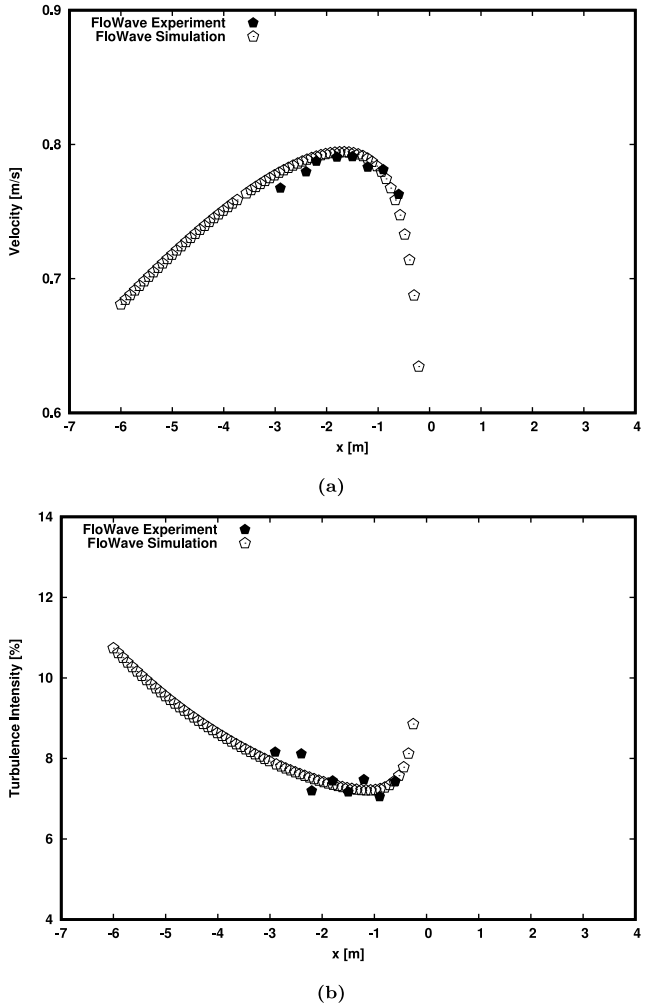

Fig. 18. Velocity magnitude (a) and turbulence intensity (b) for single rotor plotted against x-axis location along the centre of the tank at hub height, i.e. $y = 0m$ and $z = 1m$, TSR 5.5.

front of (Fig. 18) and behind the rotor (Fig. 19) to capture the fluid characteristics upstream as well as exiting the rotor. The results of the velocity and turbulence plots in Figs. 18 and 19 demonstrate

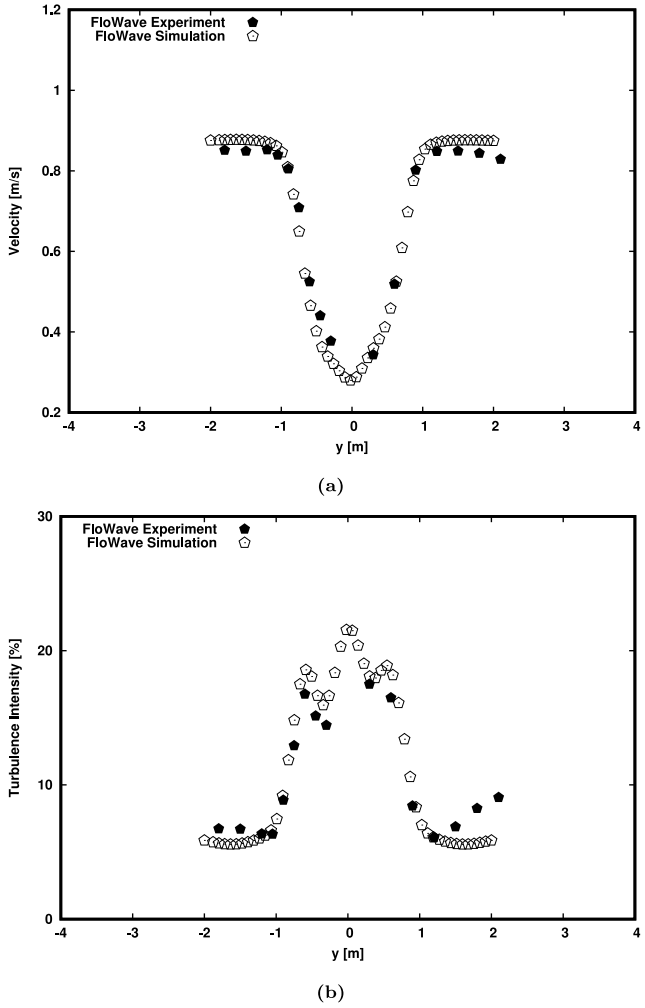

Fig. 19. Velocity magnitude (a) and turbulence intensity (b) for single rotor plotted against y-axis across the wake region, i.e. $x = 2.4m$ and $z = 1m$, TSR 5.5.

good correlation with the experimental results, especially when considering the experimental deviation associated with this type of measurement, see Ref. [6] for more information. The distribution and magnitudes of the feature set show good correlation with the experimental results; this is particularly true of the asymmetric flow structures observed. The slight asymmetry in the plots in Fig. 19 could be as a result of the interaction of the assembly structure with the fluid medium and with the swirl imparted by the rotor. This phenomena can be observed more clearly with reference to Figs. 20–22. The visualisation shows fluid emanating from the assembly structure and propagating downstream as a result of the wake rotation. The fluid mixes about the centreline of rotation a few diameters downstream (approximately 4–5 diameters). This fluid flow transports the turbulence emanating from the assembly structure (Fig. 22), which pools before dispersing at about the same distance downstream. This pooling of turbulence has also been reported by Ref. [22].

The accuracy to which the GAD-CFD approach predicts the velocity and turbulence data in Fig. 19 is within 3%–5% of the measurements.

Fig. 23 shows a characteristic asymmetric sideways "W-shaped wake" (at $X = 0$ m) as part of the fluid passes through the turbine. It can be seen from the figure that as the flow disperses further in the wake the asymmetric sideways "W-shaped wake" profiles

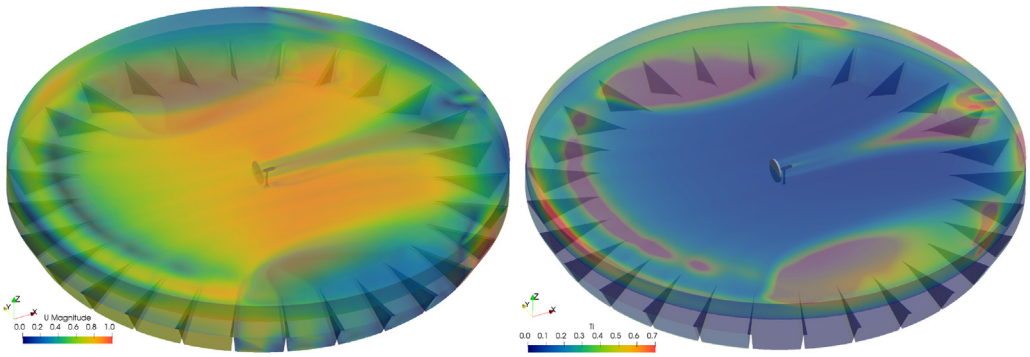

Fig. 20. Visualisation of velocity magnitude $[0 \ldots 0.9] m.s^{-1}$ through the domain (left), and turbulence intensity (right) for single rotor, TSR 5.5.

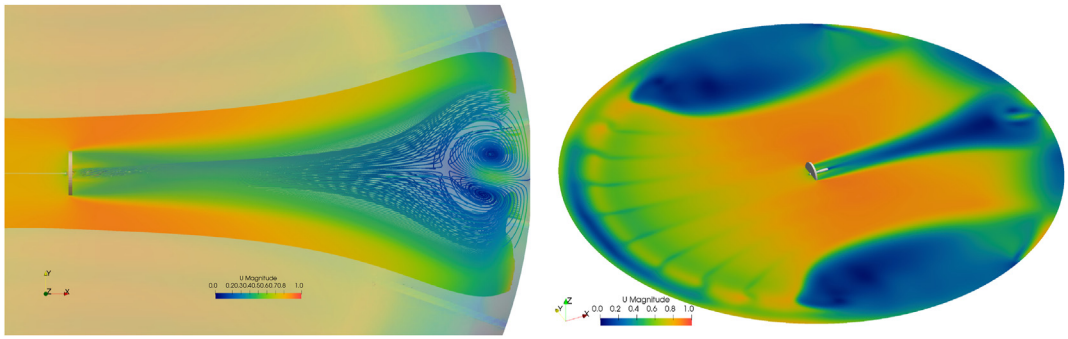

Fig. 21. Visualisation of velocity magnitude taken at hub height (1 m above the tank floor) through the domain for single rotor, TSR 5.5.

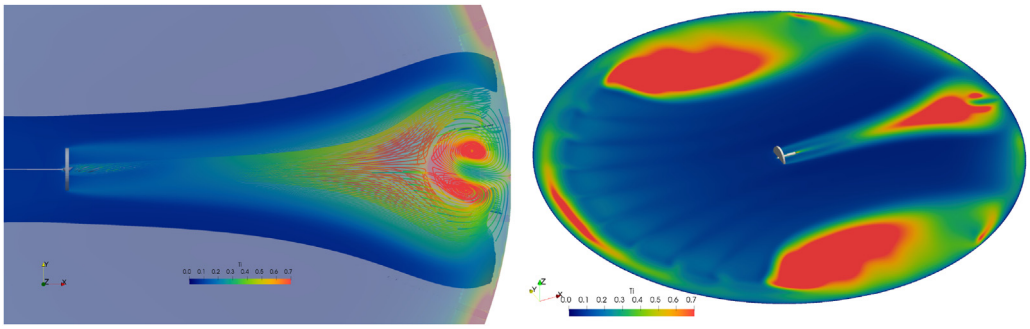

Fig. 22. Visualisation of turbulence intensity taken at hub height (1 m above the tank floor) through the domain for single rotor, TSR 5.5.

disappear. The wake profile width also becomes larger than the turbine diameter as the wake expands. Although downstream velocity measurements were only recorded for distances of up to 2.4 m in the experiment, the CFD plot taken further downstream at 4.0 m shows that rotor influence on the flow is still visible, a factor which must be taken into account when choosing sites to deploy further rotors.

6.3. FloWave three rotors

A view of the turbine influence on the inflow is provided in Fig. 24a for the three-turbine array model taken along the centreline of the primary rotor in the streamwise direction. Results of the tank only (TANK) and single rotor (SR) cases have been included for comparison purpose. For all cases with turbines in the tank, there is an inflow deficit of between 0.01 and 0.03 m/s compared with tank only case. This is most pronounced for the three-turbine array case. The impact of the turbines on the inflow is well captured in terms of

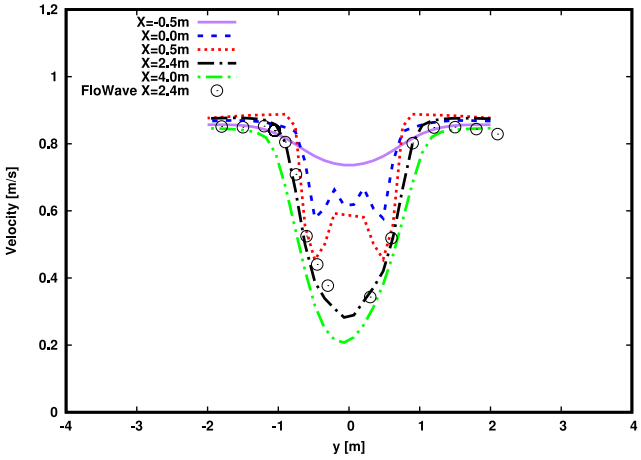

Fig. 23. Velocity magnitude transects taken at hub height, i.e. $y = 0$ and $z = 1$ for single rotor, TSR = 5.5.

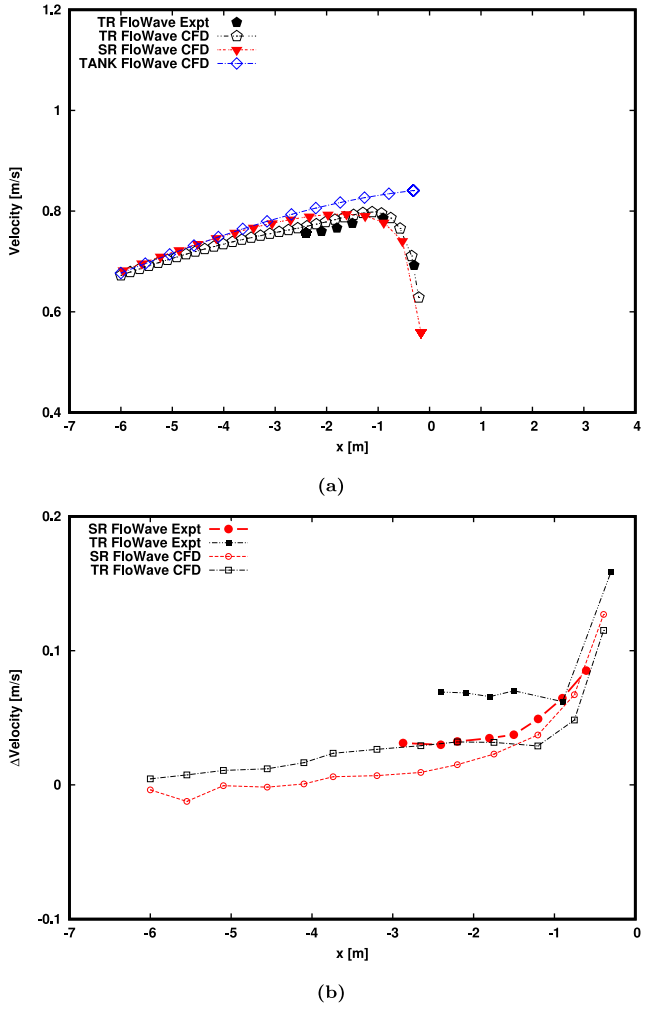

Fig. 24. Velocity magnitude for three rotors, TR, including baseline tank only, TANK and single rotor, SR (a) and mean velocity relative to empty baseline tank only (b) plotted against x-axis location along the centre of the tank at hub height, i.e. $y = 0$ and $z = 1$, TSR = 7.0 for the three-rotor array model.

Table 5
Predicted C_P and C_T for the primary turbine, *R*0 in the three-rotor array, $TR = 7$. The two upstream turbines, *R*1 and *R*2 have been included for comparison purpose.

Parameter	$R0_{EXP}$	$R0_{CFD}$	$R1_{CFD}$	$R2_{CFD}$
C_P	0.3617	0.3287	0.2897	0.2920
C_T	0.7545	0.7836	0.7864	0.7423

the mean velocity relative to empty baseline tank (Fig. 24b). There is however a downward shift of the mean velocity curves and does not significantly change the mean velocity curve slope. Since the turbine forces are dependent on the inflow conditions, slight over or under-prediction in velocity and turbulence intensity to the turbines will result in increased or decreased turbine forces as can be seen in Table 5. The applied GAD-CFD approach captures the profile of turbulence intensity in Fig. 25 extremely well, with differences of less than 5% compared to the FloWave measurements.

Table 5, demonstrates the performance of the primary turbine in the array model in terms of *CP* and *CT* at TSR = 7. GAD-CFD predicts the thrust and power within 3.5% and 9.5% respectively. Figs. 26–28 highlights the difference in wake structure of the primary turbine in the three-rotor array model in contrast to the single rotor case in

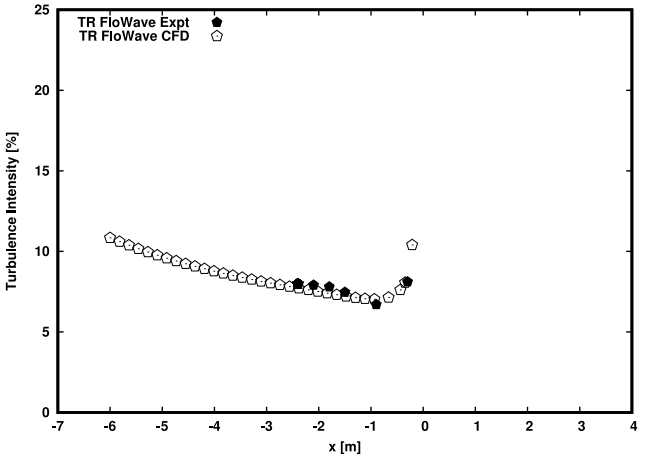

Fig. 25. Turbulence intensity for three rotors only plotted against x-axis location along the centre of the tank at hub height, i.e. $y = 0$ and $z = 1$, TSR = 7.0 for the three-rotor array model.

Figs. 20–22. The primary rotor in the three-rotor array model falls within a higher velocity region, resulting from flow acceleration occurring between the two upstream rotors. It appears the lateral spacing between the two upstream rotors may have played a role in the primary turbine benefitting from the accelerated approaching flow. Having higher velocities approaching the turbine can result in an increase in the extractable power. This is also supported by Ref. [18] who investigated the influence of lateral spacing on tidal stream turbine array layouts. The authors showed that having smaller lateral spacing (e.g. less than 1.5D) between two upstream turbines in a three-turbine array can usually result in a reduction in centreline velocities. Values between the two rows of turbines can also result in values below freestream velocity, hence lower velocities approaching the downstream rotor. This can reduce the turbine performance.

Line samples of the velocity and turbulence data (Fig. 29) were taken behind the primary rotor in the three-rotor array to capture the fluid characteristics exiting the rotor. The results of the velocity and turbulence plots of the primary turbine demonstrate reasonable correlation with the experimental results. However, slight deflection of the wake is noticeable in the profile of the two upstream turbines. Such deflections are mainly characteristic of yawed turbines as reported by Ref. [49]. It should be recalled that there were slight variations in mean flow and turbulence intensity present across the tank area in the tank only results. These could have contributed to the deflections observed in the upstream turbines.

To investigate the flow regime in the region between the turbines, a series of line samples of the velocity were taken close to the tank floor, at hub height and at the water surface. Fig. 30 shows the locations where the line samples were taken along with turbine/blade positions. In all cases (Fig. 31a–f and 32 a-f), the trend in the upstream velocities are similar with very little differences between them. However, a closer inspection of the plots show slightly lower velocities approaching the primary rotor in the three-rotor array compared to the tank only baseline and single rotor cases. Notice also how the rotor influence on the inflow can be observed close to the tank floor at $z = 0.1m$ and at the water surface $z = 2m$.

The differences in the velocity plots become visible downstream of the primary rotor in the array model. Close to the tank floor (in Fig. 31a&d and 32a&d) and the water surface (in Fig. 31c&f and 32c&f) in the near wake region, the flow velocities are marginally faster, compared to the empty tank baseline and the single rotor

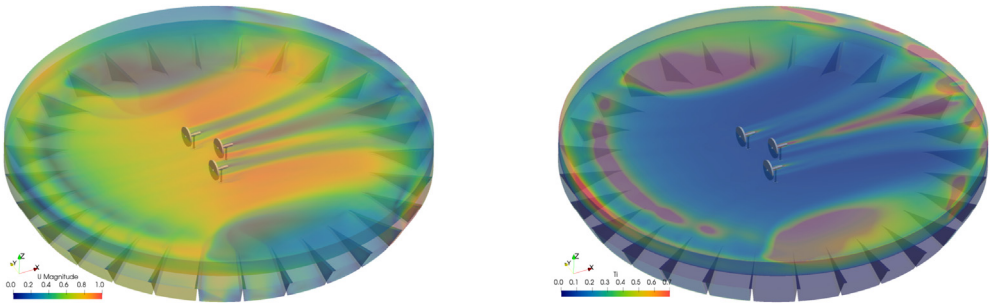

Fig. 26. Visualisation of velocity magnitude $[0 \ldots 0.9] m.s^{-1}$ through the domain (left), and turbulence intensity (right) for three rotors, TSR 7.0.

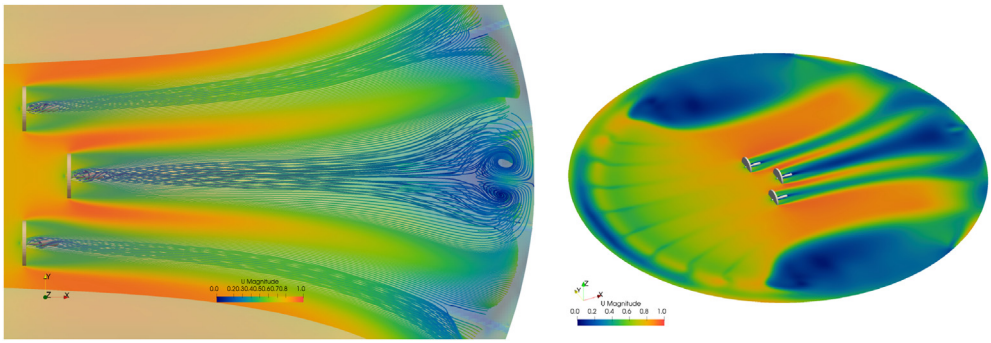

Fig. 27. Visualisation of velocity magnitude taken at hub height (1 m above the tank floor) through the domain for three rotor, TSR 7.0.

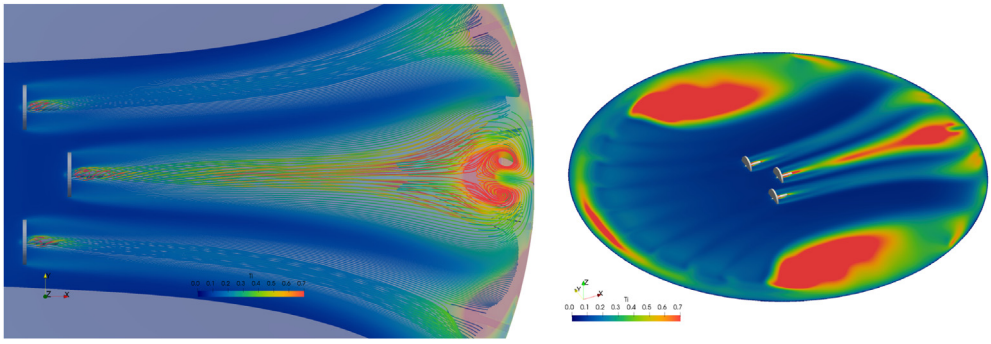

Fig. 28. Visualisation of turbulence intensity taken at hub height (1 m above the tank floor) through the domain for three rotor, TSR 7.0.

cases. At the hub height and in the near wake region, the flow does not come under much influence of the turbine in the case of the single turbine as shown in Fig. 31b. While in the three-turbine case it does and the flow speed rise can be attributed to the flow acceleration between the front two turbines. As the flow approaches the primary turbine's blade location in Figs. 31e and 32b&e, significant wake deficit is observed, increasing for the three turbine array case.

The GAD-CFD approach is also evaluated for the prediction of the transverse profile of streamwise velocity downstream of the array model in Fig. 33. Close to the primary rotor, the velocity fields are significantly asymmetric in the near wake region at $x = 0m$ to $x = 0.5m$, with reducing asymmetry as mixing occurs further downstream at $x = 2.4m$ and $x = 4.0m$. It is interesting to note how the shape differs from that of the single rotor in Fig. 23. At $x = 2.4m$ the GAD-CFD gives a good prediction of the velocity behind both upstream rotors.

7. Discussion

The results of GAD-CFD model simulations incorporating multiple configurations of tidal turbine rotors have been compared to high resolution test-tank measurements. A summary of the data analyses is presented below for the three cases: the tank-only (numerical test-tank) model; the single-rotor case; and the triple-rotor case.

7.1. Baseline tank-only model

Based on the comparison and level of agreement of the modelled flow-field to that measured at FloWave (in the regions of interest for this study) it has been shown that it is not necessary to model the tank in its entirety i.e. from the inlet/outlet vent only. This result reduces the modelling complexity significantly and provided a baseline from which to incorporate energy conversion devices.

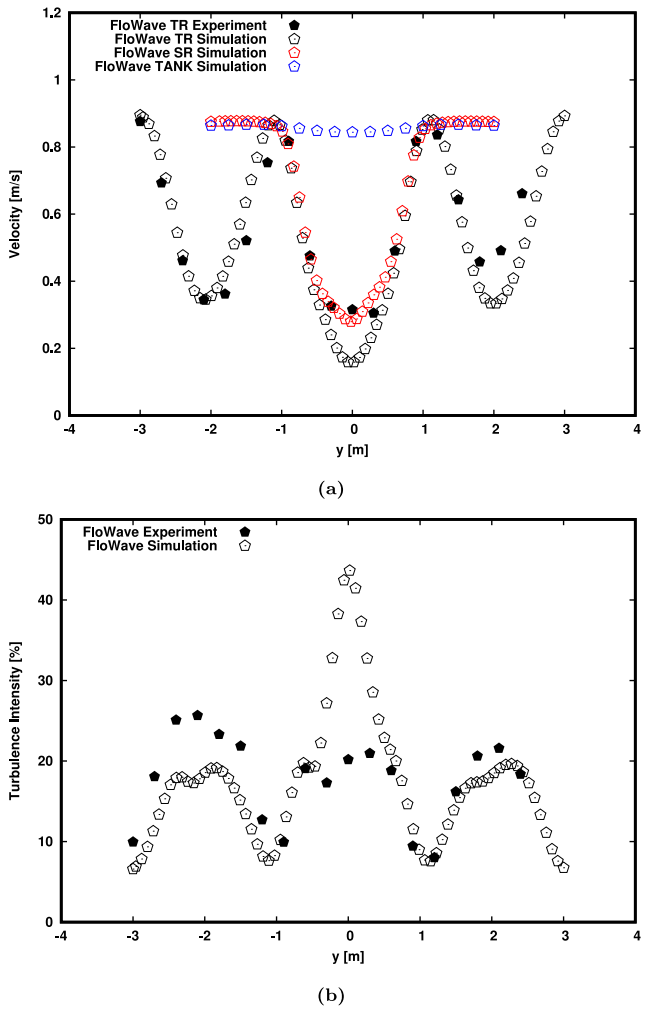

Fig. 29. Velocity magnitude for three rotors, TR, including baseline tank only, TANK and single rotor, SR (a) and turbulence intensity for three rotors only (b)plotted against y axis location along the centre of the tank at hub height, i.e. $x = 2.4$ and $z = 1$, TSR = 7.0 for the three-rotor array model.

All computed velocity plots compared very well with the experimental results with the exception of the lateral profiles of streamwise velocities and turbulence intensities where slight differences between the simulation and experiment was observed. This was attributed to difficulty in controlling individual impeller units in the tank to generate the required flow across the test area during the experiment, which may have resulted in some variation in mean flow and turbulence intensity across the tank area.

With further validation e.g., higher density and coverage of in-situ measurements, multiple new opportunities for combined physical-numerical work are enabled. For example, where there are notable discrepancies at specific regions of the domain in the predicted to measured tank behaviour further investigation can be carried out on root causes, leading to either improved numerical simulation or optimised tank operation and ultimately to a validated numerical representation of a unique test facility.

7.2. Single rotor model

For the single rotor case, the distribution of power and thrust correlate well with the experimental results, with differences of less than 0.05% and 12% respectively at TSR = 5.5. A slight over

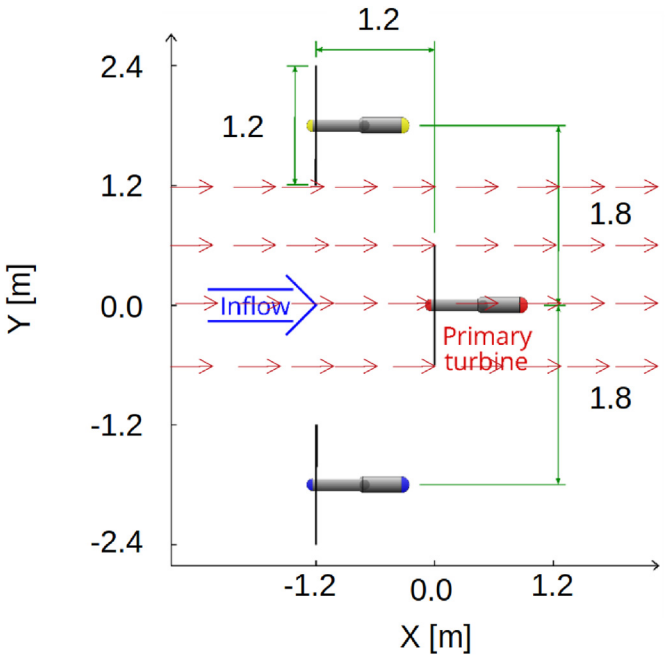

Fig. 30. Line sample locations (red arrows) for streamwise velocity extraction showing turbine/blade position.

prediction of thrust, especially at TSR > 5 and an under prediction of power was observed in the C_P curve. The GAD-CFD model only reports thrust acting directly on the rotor, thus a correction needs to be calculated considering the fluid drag acting on the assembly. This has also been examined in Ref. [46] and demonstrates good correlation for the combined results of thrust. RANS based models, of which the GAD-CFD model is, are known to under-predict how much of the energy exerted on the turbine will be converted into rotation on the blades and hence useful power. This has also been reported by Refs. [47,48]. Another drawback of the GAD-CFD model is that it fails to effectively predict local flow details at the turbine blades and could also contribute to the C_P under-prediction. With this in mind the thrust and power characteristics correlate well and show a similar trend to the observations of the experimental results.

Line samples of velocity and turbulence data were also taken in front and behind the rotor to capture the fluid characteristics upstream as well as exiting the rotor. The results showed good correlation with the experiment. The asymmetry seen in the wake plots were as a result of the interaction of the assembly structure with the fluid medium and with the swirl imparted by the rotor. Fluid emanating from the assembly structure propagates downstream as a result of the wake rotation. The fluid then mixes about the centreline of rotation a few diameters downstream. The fluid flow transports turbulence emanating from the assembly structure, which pools before dispersing at about the same distance downstream. The pooling of turbulence has also been reported by Ref. [22]. Although the wake velocities were recorded for a shorter distance downstream of the rotor, the influence of the rotor on the flow was visible further away in the wake. This is very important to consider especially when choosing sites to deploy further rotors.

The upstream and wake characteristics of the single rotor was predicted to within 3–5% of the measured data.

7.3. Triple rotor model

For the triple rotor case, variation of thrust and power

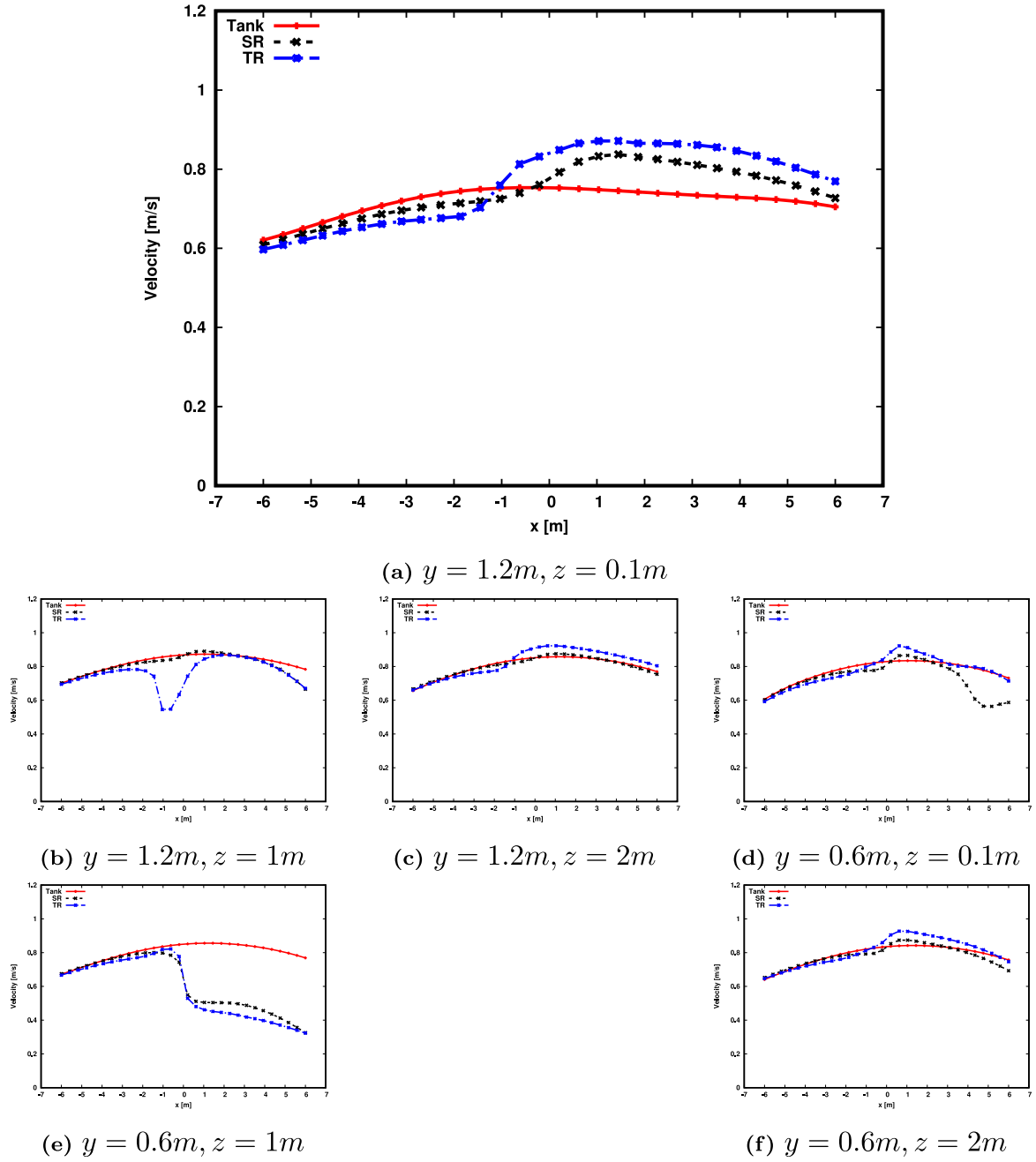

Fig. 31. Variation of flow between turbine locations using GAD-CFD, i.e. U at points on two streamwise transects ($y = 1.2m$ and $y = 0.6m$) and at $z = 0.1m$ to $z = 2m$ above tank floor.

coefficient with tip-speed ratio was consistent with measurements with differences of less than 3.5% and 9.5% respectively at TSR = 7.0. Asymmetry within the wake structure of the three-turbine array configuration was observed as a result of the wake interacting with the tower structure. The GAD-CFD model showed that the primary rotor benefitted from the flow acceleration from the two rows of turbines, resulting in high velocity flow approaching the primary turbine thus increasing the extractable power. The results of the experimental test described in this paper substantiates this finding.

The transverse profile of streamwise velocity downstream of the three-turbine array model showed distinct individual wakes close to the rotor, whilst the wakes merged further downstream. The velocity and turbulence intensity profiles behind both upstream rotors were also predicted reasonably well.

7.4. Computational efficiency

The model run times vary between approximately 1.5 to 3.0 wall clock hours for the single rotor computations and 4.5 to 6.0 wall clock hours for the array model for each TSR point. These timings depend on the size of the domain (quantity of cells), and the hardware capabilities (processing speed), and speed of convergence. The computations were run on 10 processors using the Astute cluster at the University of Swansea. These model run times are a significant improvement over the use of fully resolved turbine geometry models. A sliding grid transient model of a single rotor case with fully resolved hydrofoil geometry would require a mesh size of at least 20 million elements to maintain an appropriate y^+. This is in contrast to the approximately 6 million elements used for

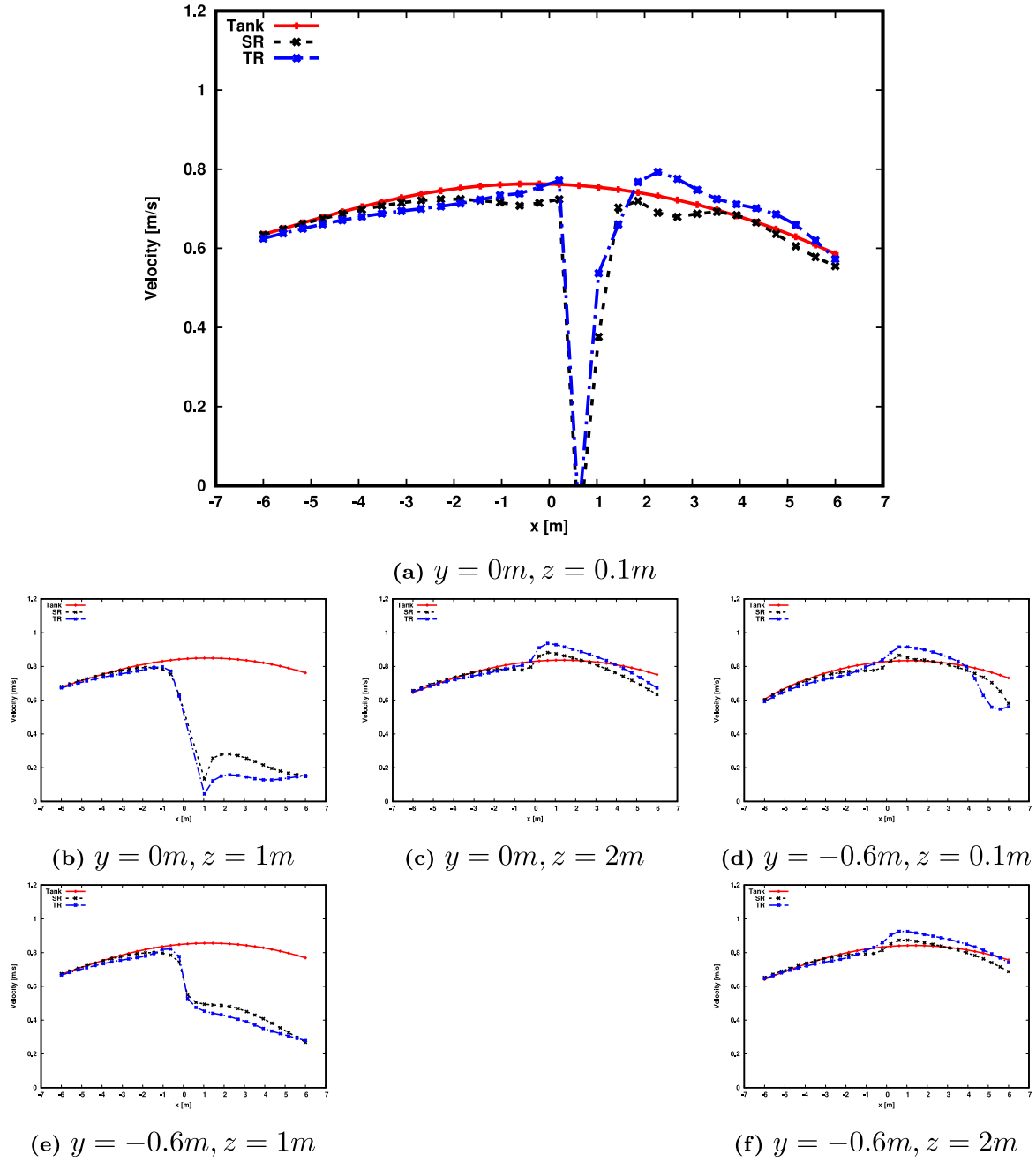

Fig. 32. Variation of flow between turbine locations using GAD-CFD, i.e. U at points on two streamwise transects ($y = 0.0m$ and $y = -0.6m$) and at $z = 0.1m$ to $z = 2m$ above tank floor.

the single rotor. The reason for the additional cell count is due to the amount of refinement required at the hydrofoils to correctly capture the lift and drag characteristics. This is also combined with the time step size needed to maintain an acceptable Courant number. For instance, with a simulation time of approximately 20 min per time step, would require a minimum simulation time of approximately 480 wall clock hours on the same hardware. Therefore, a complete TSR sweep would take approximately 1920 wall clock hours for this reference case on reference hardware.

8. Conclusions

An efficient method for simulating tidal stream energy converter rotor response to realistic inflow conditions and capturing the subsequent impact to far-field flow structure using a GAD-CFD approach has been demonstrated. Model validation against experimental testing has been conducted and was made possible by coordinating a replicate physical tank-testing experiment during experimental design.

The results show that the GAD-CFD model gives a better representation of the rotor's downstream wake characteristics, particularly with the inclusion of an accurate representation of the assembly structure. Slight discrepancy was found in the rotor forces owing to the failure of the model to better predict local details at the blades which can influence loadings on the turbine. The model also only reports thrust directly acting on the rotor, thus a

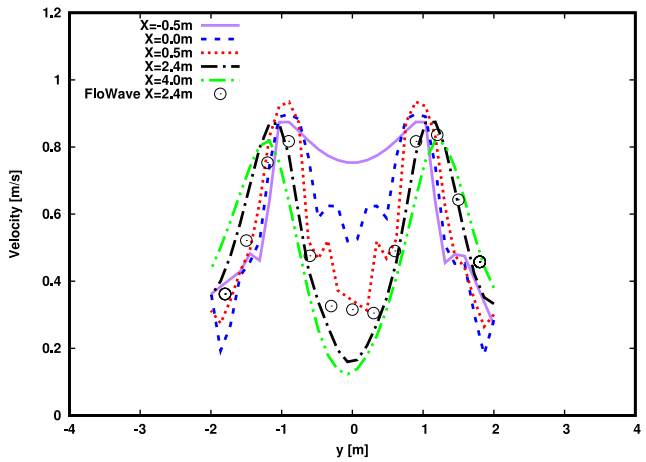

Fig. 33. Velocity magnitude transects taken at hub height, i.e. $y = 0$ and $z = 1$ for triple rotor, TSR = 7.0.

correction needs to be calculated considering the fluid drag acting directly on the structure. Further validation of the model would be recommended as more experimental data becomes available and the model improved to account for such details. However, the study provides confidence that the approach can be applied to a range of scenarios; both laboratory scale flume studies, and large scale deployments in both the marine and wind environments. Due to the computational efficiency, such an approach, especially when compared to fully resolved turbine geometry models, makes the GAD-CFD technique suitable for modelling arrays consisting of a large number of rotors and for conducting multiple model runs under varying tidal and machine-operating-point conditions. It is therefore appropriate to also consider the model for studying tidal stream arrays and their interaction with respect to local topography and power control. Since tidal energy could play an important role in decarbonising electricity generation it is important to have access to efficient and accurate engineering tools such as the one developed here which sits between highly detailed blade resolved models and larger scale oceanographic and atmospheric models. Improved modelling will reduce the technical risk of operating these devices in the highly energetic marine environment thus increasing economic viability of the sector.

The GAD-CFD model includes new improved features such as a more concise downwash distribution computation, variation of foil section, application of tip radius correction, variation of lift/drag curves with Reynolds number and surface roughness. The use of analytical methods to successfully and effectively predict the distribution of lift towards the tip of finite wing, are demonstrated to produce reasonable estimates of power and thrust. Allowing for the variation of foil section shape within the model adds to the refinements including the distribution of forces along the foils. This helps produce better characteristics closer to the rotor hub, and also improved prediction in the stall region of the TSR range. Tip radius correction produces an effect that is more visible at higher TSRs and this in combination with including surface roughness effects for predicted lift/drag curves reduces over estimations in the overspeed part of the TSR range.

Future work should focus on improving the model to account for changing lift and drag characteristics at higher levels of free stream turbulence. As turbulence levels increase, the quantity of lift and drag changes, as does the stall point relative to angle of attack, and post stall features significantly change. The model could be combined with turbine control algorithms that consider power capping through stall or pitch control to enable the study of rotors interacting in an array as well as exploring the impact of variable inflow conditions on varying configurations of multiple turbine. Beyond this immediate application the developers seek to develop and incorporate more realistic bathymetry characterisations, which is expected to be an important factor in real-world turbine array operation. It is the authors intention to publish the implementation of the model to enable such studies to take place.

CRediT authorship contribution statement

Charles E. Badoe: Numerical, Investigation, Numerical, Methodology, Formal analysis, and, Visualization, Writing – original draft, Writing – review & editing. **Matt Edmunds:** Numerical, Investigation, Numerical, Methodology, Formal analysis, and, Visualization, Writing – review & editing. **Alison J. Williams:** Formal analysis, and, Visualization, Writing – review & editing, Work Package Leader and Project Co-investigator. **Anup Nambiar:** Experimental, Investigation, Writing – review & editing. **Brian Sellar:** Experimental, Investigation, Writing – review & editing. **Aristides Kiprakis:** Writing – review & editing. **Ian Masters:** Writing – review & editing, All authors have read and agreed to the published version of the manuscript.

Declaration of competing interest

The authors declare that they have no known competing financial interests or personal relationships that could have appeared to influence the work reported in this paper.

Acknowledgements

This work was supported by the Engineering and Physical Sciences Research Council (EPSRC) funded “Extension of UKCMER Core Research, Industry and International Engagement” project (EP/M014738/1), and the SURFTEC SuperGen grand challenge project, funded under EPSRC grant (EP/N02057X/1) and the SELKIE project funded by the European Regional Development Fund through the Ireland Wales Cooperation programme.

References

[1] A. Bahaj, Marine current energy conversion: the dawn of a new era in electricity production, Phil. Trans. R. Soc. A. 371 (2013), 20120500.
[2] The Crown Estate, UK wave and tidal key resource areas project. http://www.thecrownestate.co.uk, 2018. Retrieved: May 2018.
[3] P. Giguere, M.S. Selig, Design of a Tapered and Twisted Blade for the NREL Combined Experiment Rotor, Tech. Rep. NREL/SR-500-26173. Mem, 1999.
[4] A.S. Bahaj, A.F. Molland, J.R. Chaplin, W.M.J. Batten, Power and thrust measurements of marine current turbines under various hydrodynamic flow conditions in a cavitation tunnel and a towing tank, Renew. Energy 32 (3) (2007) 407–426.
[5] T. Stallard, R. Collings, T. Feng, J. Whelan, Interactions between tidal turbine wakes: experimental study of a group of three-bladed rotors 371, Phil. Trans. R. Soc. A., 2013, 20120159.
[6] P. Mycek, B. Gaurier, G. Germain, G. Pinon, E. Rivoalen, Experimental study of the turbulence intensity effects on marine current turbines behaviour. Part I: one single turbine, Renew. Energy 66 (2014) 729–746.
[7] P. Mycek, B. Gaurier, G. Germain, G. Pinon, E. Rivoalen, Experimental study of the turbulence intensity effects on marine current turbines behaviour. Part II: two interacting turbines, Renew. Energy 68 (2014) 876–892.
[8] M. Edmunds, R. Malki, A. Williams, I. Masters, T.N. Croft, Aspects of tidal stream turbine modelling in the natural environment using a coupled BEM-CFD model, Int. J. Mar. Eng. 7 (2014) 20–42.
[9] W.M.J Batten, A.S. Bahaj, A.F. Molland, J.R. Chaplin, Experimentally validated numerical method for the hydrodynamic design of horizontal axis tidal turbines, Ocean Eng. 34 (7) (2007) 1013–1020.
[10] T. O'Doherty, A. Mason-Jones, D.M. O'Doherty, C. Byrne, I. Owen, Y.X. Wang, Experimental and computational analysis of a model horizontal axis tidal turbine, Proc. Euro Wave and Tidal Energy Conf. (2009) 833–841.
[11] J. McNaughton, S. Rolfo, D. Apsley, T. Stallard, P. Stansby, CFD power and load prediction on a 1 MW tidal stream turbine with typical velocity profiles from the EMEC test site, in: Proc of the 10th Euro Wave and Tidal Energy Conf,

2013.
[12] A. Mason-Jones, D.M. O'Doherty, C.E. Morris, T. O'Doherty, C. Byrne, P.W. Prickett, R.I. Grosvenor, I. Owen, S. Tedds, R. Poole, Non-dimensional scaling of tidal stream turbines, Energy 44 (2012) 820–829.
[13] T. Nishino, R. Willden, Two-scale dynamics of flow past a partial cross-stream array of tidal turbines, J. Fluid Mech. 730 (2013) 220–244.
[14] S. Draper, A. Borthwick, G. Houlsby, Energy potential of a tidal fence deployed near a coastal headland, Phil. Trans. R. Soc. A. 371 (2013), 20120176.
[15] M.E. Harrison, W.M.J. Batten, A.S. Bahaj, A blade element actuator disc approach applied to tidal stream turbines, Oceans (2010) 1–8.
[16] S.R. Turnock, A.B. Phillips, R. Nicholls-Lee, J Banks, Modelling tidal current turbine wakes using a coupled RANS-BEMT approach as a tool for analysing power capture of arrays of turbines, Ocean Eng. 38 (11–12) (2011) 1300–1307.
[17] A. Olczak, T. Stallard, T. Feng, P.K. Stansby, Comparison of a RANS blade element model for tidal turbine arrays with laboratory scale measurements of wake velocity and rotor thrust, J. Fluid Struct. 64 (2016) 87–106.
[18] R. Malki, A. Williams, I. Masters, T. Nick Croft, Planning tidal stream turbine array layouts using a coupled blade element momentum–computational fluid dynamics model, Renew. Energy 63 (2014) 46–54.
[19] R. Malki, A. Williams, I. Masters, M. Togneri, T. Nick Croft, A coupled blade element momentum-Computational fluid dynamics model for evaluating tidal stream turbine performance, Appl. Math. Model. 37 (2013) 3006–3020.
[20] M. Edmunds, A. Williams, I. Masters, Power shedding from stall and pitch controlled tidal stream turbines, in: Proc of 11th Euro Wave and Tidal Eng Conf., 2017.
[21] I. Masters, R. Malki, A. Williams, T. Nick Croft, The influence of flow acceleration on tidal stream turbine wake dynamics: a numerical study using a coupled BEM-CFD model, Appl. Math. Model. 37 (2013) 7905–7918.
[22] M. Edmunds, A. Williams, I. Masters, A. Banerjee, J.H. VanZwieten, A Spatially Nonlinear Generalised Actuator Disk Model for the Simulation of Horizontal Axis Wind and Tidal Turbines, Energy., 2020, p. 194.
[23] University of Edinburgh, Flowave Ocean energy Research facility. https://www.flowavett.co.uk/, 2018. Retrieved: May 2018.
[24] D. Ingram, R. Wallace, A. Robinson, I. Bryden, The design and commissioning of the first, circular, combined current and wave test basin, Proc. Oceans (2014) 1–7.
[25] S. Draycott, T. Davey, D.M. Ingram, A. Day, L. Johanning, The SPAIR method: isolating incident and reflected directional wave spectra in multidirectional wave basins, Coast. Eng. 114 (2016) 265–283.
[26] A. Robinson, I. Bryden, D. Ingram, T. Bruce, The generation of 3D flows in a combined current and wave tank, Ocean Eng. 93 (2015) 1–10.
[27] D.R. Noble, T. Davey, H.C.M. Smith, P. Kaklis, A. Robinson, T. Bruce, Characterisation of spatial variation in currents generated in the Flowave Ocean energy Research facility, in: Proc of 11th Euro Wave and Tidal Eng Conf., 2015, pp. 1–8.
[28] B.G. Sellar, G. Wakelam, D.R.J. Sutherland, D.M. Ingram, V. Venugopal, Characterisation of tidal flows at the European marine energy centre in the absence of ocean waves, Energies 11 (2018) 176.
[29] D.R.J. Sutherland, D.R. Noble, T. Davey, J. Steynor, T.A.D. Davey, T. Bruce, Characterisation of current and turbulence in the Flowave Ocean energy Research facility, Ocean Eng. 139 (2017) 103–115.
[30] D.R. Noble, S. Draycott, A. Nambiar, B.G. Sellar, J. Steynor, A. Kiprakis, Experimental assessment of flow, performance, and loads for tidal turbines in a closely-spaced array, Energies 13 (2020), 1977.
[31] S.G. Parkinson, W.J. Collier, Model validation of hydrodynamic loads and performance of a full-scale tidal turbine using Tidal Bladed, Int. J. Mar. Eng. 16 (2016) 279–297.
[32] MeyGen Ltd, MeyGen Tidal Energy Project Phase 1. Project Environmental Monitoring Programme, Technical Report, Tech. Rep. MEY-1A-70-HSE-018-I-PEMP, 2016.
[33] G.S. Payne, T. Stallard, R. Martinez, Design and manufacture of a bed supported tidal turbine model for blade and shaft load measurement in turbulent flow and waves, Renew. Energy 107 (2017) 312–326.
[34] R. Martinez, G.S. Payne, T. Bruce, Preliminary results on the effects of oblique current and waves on the loadings and performance of tidal turbines, in: Proc of the 12th European Wave and Tidal Energy Conference, EWTEC, 2017.
[35] New Civil Engineer, The MeyGen Tidal Scheme Project, Retrieved, 2019. https://www.newcivilengineer.com/world-view/future-of-energy-catching-the-flow/10038276.article. (Accessed February 2019).
[36] Nortek Vectrino, Profiler Technical Specification, Nortek, Providence, RI, USA, 2013.
[37] T. Mori, K. Naganuma, R. Kimoto, R. Yakushiji, S. Nagaya, Hydrodynamic and hydroacoustic characteristics of the flow noise simulator 2, Proc of 5th ASME-JSME Joint Fluids Eng Conf, 2007, pp. 121–127.
[38] D.G. Goring, V.I. Nikora, Despiking acoustic Doppler velocimeter data, J. Hydraul. Eng. 128 (2002) 117–126.
[39] H.G. Weller, G. Tabor, H. Jasak, C. Fureby, A tensorial approach to computational continuum mechanics using object-oriented techniques, Comp. Physics. 12 (6) (1998) 620–631.
[40] V. Yakhot, S. Orszag, S. Thangam, T. Gatski, C. Speziale, Development of turbulence models for shear flows by a double expansion technique, Phys. Fluids 7 (1992) 1510–1520.
[41] R. Griffiths, M. Woollard, Performance of the optimal wind turbine, Appl. Energy 4 (1978) 261–272.
[42] J. Anderson, Fundamentals of Aerodynamics, No. 5 in Anderson Series, McGraw-Hill Education, 2010.
[43] I. Abbott, A. Von Doenhoff, Theory of Wing Sections, Including a Summary of Airfoil Data, No. 1 in Dover Books on Aeronautical Engineering Series, Dover Publications, 1959.
[44] Airfoil Tools, Airfoil Tools, 2019. http://airfoiltools.com/. Retrieved: February 2019.
[45] Hepperle Martin, JavaFoil, 2018. https://www.mh-aerotools.de/airfoils/javafoil.htm. Retrieved: August 2018.
[46] M. Edmunds, A. Williams, I. Masters, T.N. Croft, An enhanced disk averaged CFD model for the simulation of horizontal axis tidal turbines, Renew. Energy 101 (2017) 67–81.
[47] T. Ebdon, T. O'Doherty, A. Mason-Jones, D.M. O'Doherty, Simulating marine current turbine wakes with advanced turbulence models, in: Proc of the 3rd Asian Wave and Tidal Energy Conf, 2016.
[48] W.M.J. Batten, M.E. Harrison, A.S. Bahaj, Accuracy of the actuator disc-RANS approach for predicting the performance and wake of tidal turbines 371, Phil. Trans. R. Soc. A., 2013, 20120293.
[49] P.K. Modali, A. Vinod, A. Banerjee, Towards a better understanding of yawed turbine wake for efficient wake steering in tidal arrays, Renew. Energy 177 (2021) 482–494.